

¹ Contents

²	1	Introduction	3
³	2	Pixel detectors	6
⁴	2.1	Signal formation	6
⁵	2.2	Charge Coupled Devices	8
⁶	2.3	Hybrid pixels	9
⁷	2.4	CMOS MAPS and DMPAS	11
⁸	2.4.1	DMAPS: large and small fill factor	12
⁹	2.4.2	A modified sensor	14
¹⁰	2.5	Analog front end	16
¹¹	2.5.1	Preamplifier	16
¹²	2.6	Readout logic	17
¹³	3	Use of pixel detectors	21
¹⁴	3.1	Tracking in HEP	21
¹⁵	3.1.1	Hybrid pixels at LHC and at SuperKEKB	23
¹⁶	3.1.2	First attempts to MAPS	26
¹⁷	3.2	Other applications	29
¹⁸	3.2.1	Applicability to FLASH radiotherapy	30
¹⁹	4	TJ-Monopix1	36
²⁰	4.1	The sensor	38
²¹	4.2	Front end	40
²²	4.2.1	ALPIDE-like	41

23	4.3 Readout logic	42
24	5 Arcadia-MD1	47
25	5.1 The sensor	47
26	5.2 Readout logic and data structure	48
27	5.2.1 Matrix division and data-packets	48
28	6 Characterization	51
29	6.1 TJ-Monopix1 characterization	51
30	6.1.1 Threshold and noise: figure of merit for pixel detectors	51
31	6.1.2 Linearity of the ToT	56
32	6.1.3 Calibration of the ToT	58
33	6.1.4 PMOS flavor: changing the bias	62
34	6.1.5 Measurements with radioactive sources	63
35	6.1.6 Dead time measurements	65
36	6.2 ARCADIA-MD1 characterization	67
37	7 Test beam measurements	68
38	7.1 Apparatus description	69
39	7.1.1 Accelerator	69
40	7.1.2 Mechanical carriers	70
41	7.2 Measurements	71
42	7.2.1 MIP spectrum using cosmic rays as source	77
43	A Pixels detector: a brief overview	79
44	A.1 Radiation damages	79
45	Bibliography	83
46	Characterization of monolithic CMOS pixel sensors for charged particle detectors and	
47	for high intensity dosimetry	

⁴⁸ **Chapter 1**

⁴⁹ **Introduction**

⁵⁰ Since the 1980s, when the fabrication of device with very small electrodes (50-100 μm)
⁵¹ became a practical possibility, pixel detectors have been widely employed for imaging and
⁵² tracking charged particles in the vertex region of experiments at accelerators. Thanks to
⁵³ their excellent spatial resolution, today even better than 10 μm , they allow for true three-
⁵⁴ dimensional space-point determination even at high particle fluxes and in particular for
⁵⁵ the identification of secondary vertices of short-lived particles such as τ and B mesons. Re-
⁵⁶ quirement imposed by accelerator are stringent and they will become even more with the
⁵⁷ increase of luminosity; in this scenario CMOS Monolithic Active Pixel Sensors (MAPS),
⁵⁸ based on the technology of CMOS cameras, are being developed to improve the perfor-
⁵⁹ mance of the hybrid pixel detectors, which currently constitute the state-of-art for large
⁶⁰ scale pixel detector, in particular by reducing the amount of material, power consumption
⁶¹ and pixel dimension. Indeed, while hybrid pixels are made by two parts, the sensor and
⁶² the electronics, welded together through microconnection, the MAPS integrate them all
⁶³ on the same wafer.

⁶⁴ Experiments such as ALICE at LHC and STAR at RHIC have already introduced the
⁶⁵ CMOS MAPS technology in their detectors. ALICE Tracking System (ITS2), upgraded
⁶⁶ during the LHC long shut down in 2019-20, was the first large-area ($\sim 10 \text{ m}^2$) silicon vertex
⁶⁷ detector based on CMOS MAPS. Thanks to the reduction of the material budget, ITS2,
⁶⁸ which uses the ALPIDE chip developed by ALICE collaboration, obtained an amazing im-
⁶⁹ provement both in the position measurement and in the momentum resolution, improving
⁷⁰ the efficiency of track reconstruction for particle with very low transverse momentum (by

71 a factor 6 at $p_T \sim 0.1$ GeV/c). Further advancements in CMOS MAPS technology are
72 being aggressively pursued for the ALICE ITS3 and the Belle II vertex detector upgrades
73 (both foreseen around 2026-27) and by the R&D53 collaboration for the upgrade at HL-
74 LHC, with the goals of further reducing the sensor thickness and improving the readout
75 speed of the devices, while keeping power consumption at a minimum.

76 Beside tracking, the development of pixel detectors is a very active field with many
77 applications: a noteworthy example of detector originally used in particle physics, and
78 later employed mainly for medical imaging, but also in space and for art authentication, is
79 Medipix, a hybrid system developed at CERN within the Medipix collaboration. Among
80 medical applications, a possible use of CMOS MAPS could be in dosimetry: in the last few
81 years the search of radiotherapy oncological treatments with high intensity beams (FLASH
82 mode) is requiring new dosimeters, both for the therapies as well as new beam-monitors
83 (especially for focused very high energy electron beams), which are capable of deal with
84 extreme dose rate (up to 40 Gy/s).

85 I have studied the characteristics of two ALPIDE-like CMOS MAPS chips and tested
86 them under different front end configuration. The first chip, the TJ-Monopix1 from the
87 Monopix series, is a TowerJazz MAPS fabricated in 180 nm CMOS technology with an
88 active area of $1 \times 2\text{cm}^2$ (448×224 pixels) and is one of the prototypes for the Belle II vertex
89 detector upgrade. The second chip, called Main Demonstrator-1, has an active area of
90 $1.28 \times 1.28\text{cm}^2$ (512×512 pixels) is produced by LFoundry in 110 nm CMOS technology
91 and designed by the ARCADIA (Advanced Readout CMOS Architectures with Depleted
92 Integrated sensor Arrays) group; it is intended to be a general purpose device with possible
93 use in medical scanners, space experiments, future lepton colliders and also possibly X-ray
94 applications with thick substrates. The main differences between the two chips are in the
95 output signal type and in the readout sequence of the matrix. Concerning the former
96 point TJ-Monopix1 returns an analog output information, that is the time over threshold
97 of the pulse which can be related with the charge released by the particle in the sensor,
98 while MD1 returns only a digital information; regarding the latter, instead, TJ-Monopix1
99 has a completely sequential readout, while MD1 grossly combines the information of the
100 hits before the readout in order to reduce the data transmission time.

101 I have set up two test systems for the two chips in the INFN clean laboratories and
102 characterized the devices electrically, with measurement related with the front end, the
103 threshold, the noise and the dead time. The mean minimum stable threshold evolved
104 through different generation of chips and at nowadays chips it is less than 500 e^- , allowing
105 thinner sensors with smaller signals: TJ-Monopix1 has proven to be in agreement with
106 this, having a threshold of $\sim 400\text{ e}^-$ to be compared with the 2 ke^- signal expected in
107 an epitaxial layer of $25\text{ }\mu\text{m}$. However this moving down requires a **rumore basso, $\sim\text{e}^-$ in**
108 **TJ-Monopix1.** Moreover, since one of the main challenges of MAPS are the differences
109 between pixels, due to process parameters variation across the wafer, which make the
110 sensor response nonuniform, I have measured the threshold and noise dispersions across
111 the matrix, **numeri**. All these measurements are important to verify the design parameters
112 of the chip comparing the results with the values obtained by the simulation. Moreover
113 I have studied the response of the analog signal recorded by TJ-Monopix1, that is the
114 time over threshold, and in order to have an absolute value in electrons of it, I performed
115 an calibration using a Fe55 x-ray source. Then, we have tested TJ-Monopix1 at very high
116 intensity using the electron beam of the ElectronFlash accelerator recently installed at
117 Santa Chiara hospital in Pisa; up to now I have participated in the design of the setup
118 needed for test beam measurement, **while the analysis of the data are going on besides a**
119 **simulation of the going on.**

₁₂₀ **Chapter 2**

₁₂₁ **Pixel detectors**

₁₂₂ Pixel detectors are semiconductor detectors which are segmented in two dimensions: this
₁₂₃ distinguish them from the strip detectors, such that a single plane of detector already
₁₂₄ provides both the coordinates of impact of the detected particle. Their operation is based
₁₂₅ on the p-n junction (fig. 2.1). A p-n junction is built by bringing in contact two n
₁₂₆ and p doped silicon crystals. At the boundary, recombination of both charge carriers
₁₂₇ occurs forming a region, the depletion zone, which is free of charge carriers. The charged
₁₂₈ donors⁺ and acceptor⁻, that remain ionised in the n-type and p-type regions, features a
₁₂₉ space charge and create an electric field across the junction, causing a drift current in the
₁₃₀ opposite direction to the diffusion one, through which the junction reaches an equilibrium
₁₃₁ state. Assuming a constant space change, the electric field is linear and reach a maximum
₁₃₂ at the boundary of the *p* and *n* layers.

₁₃₃ **2.1 Signal formation**

₁₃₄ When a charged particle passes through a pixel and loses energy by ionization only a
₁₃₅ part of that energy is used to generate electron-hole pairs, since another part is used for
₁₃₆ other processes, as lattice excitation. The average energy needed to create a pair at 300 K
₁₃₇ in silicon is $w_i = 3.65 \text{ eV}$, that is more than the mean ionization energy because of the
₁₃₈ interactions with phonon, since for a minimum ionizing particle (MIP) the most probable
₁₃₉ value (MPV) of charge released in the semiconductor is $0.28 \text{ keV}/\mu\text{m}$, hence the number

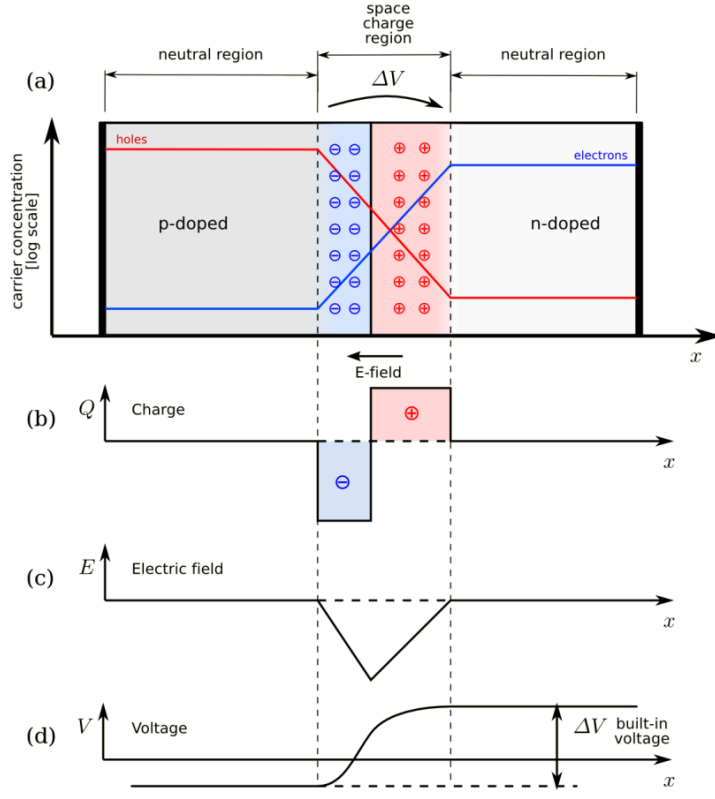


Figure 2.1: The structure of a p-n junction. (a) structure, (b) space charge density, (c) electric field distribution and (d) potential distribution.

¹⁴⁰ of electrons-vacuum pairs is:

$$\langle \frac{dE}{dx} \rangle \frac{1}{w_i} \sim 80 \text{ e/h} \sim \frac{1.28 \cdot 10^{-2} fC}{\mu m} \quad (2.1)$$

¹⁴¹ Because of the splitting of the energy depositon between the two different processes, the
¹⁴² number $N_{e/h}$ of couples generated undergoes fluctuations that usually follow a Poisson
¹⁴³ distribution; thus the fluctuations of $N_{e/h}$ is equal to $\sigma_{e/h} = \sqrt{N_{e/h}}$. Under the constraint
¹⁴⁴ of complete absorption of a particle, the energy resolution improves of a factor \sqrt{F} , where
¹⁴⁵ F is called the Fano factor and determines the ultimate limit of energy resolution for
¹⁴⁶ semiconductors. F is a function of the material and temperature and for silicon is equal
¹⁴⁷ to ~ 0.115 .

¹⁴⁸ In order to avoid a loss signal, it is fundamental that pairs e/h are produced in the
¹⁴⁹ depleted region of the semiconductor, where the probability of recombination with charge
¹⁵⁰ carriers is low. For this reason pixel detectors are commonly reverse biased: a positive
¹⁵¹ bias is given to the n electrode and a negative to the p in order to grow the depletion zone

152 in the epitaxial layer within the bulk. The width of the depletion region depends on the
 153 external bias V_{ext} , the resistivity ρ and also with the dopant:

$$d_n \sim 0.55 \sqrt{\frac{\rho}{\Omega cm} \frac{V_{ext}}{V}} \mu m \quad d_p \sim 0.32 \sqrt{\frac{\rho}{\Omega cm} \frac{V_{ext}}{V}} \mu m \quad (2.2)$$

154 Thus, high resistivity wafers ($100 \Omega cm - k\Omega cm$) are typically preferred because they allow
 155 bigger depletion zone with smaller voltage bias.

156 The charges created whithin the sensor are separated by an electric field and collected
 157 at their respective electrodes (p for holes and n for electrons)¹; by the drift of these charges,
 158 a signal i_e is generated on the electrode e as stated by the Shockley-Ramo's theorem:

$$i_e(t) = -q v(t) E_{WF,e} \quad (2.3)$$

159 where $v(t)$ is the instantaneous velocity of the charge q and E_{WF} is the weighting field,
 160 that is the field obtained biasing the electrode e with 1V and all the others with 0V. The
 161 drift velocity of the charge depends on the electric field and on the mobility of the particle:

$$v = \mu(E) E \quad (2.4)$$

162 where $\mu(E)$ is a function of the electric field and is linear in E only for small E : at higher
 163 values the probability of interactions with optical phonons increases, the mobility drops
 164 and this leads to a saturation of the velocity (fig. 2.2). Typical values for electrons and
 165 holes mobility in silicon at room temperature are $\mu_n \sim 1450 \text{ cm}^2/\text{Vs}$, $\mu_h = 500$.

166 2.2 Charge Coupled Devices

167 In CCDs the charge is created in a very thin active epitaxyal layer (typically $10 \mu\text{m}$,
 168 maximally about $30 \mu\text{m}$) and then locally stored in a potential minimum which is created
 169 by a MOS structure. The size of the CCD cells is typically in the range $10 \mu\text{m}$ to $20 \mu\text{m}$
 170 such that spatial resolutions are of the order of a few micrometres. The collected charges
 171 are moved stepwise from electrode to electrode (thus so called 'bucket chain') by applying a
 172 potential with a clock with frequency of $\sim \text{MHz}$; despite of such high frequency, the readout

¹Even if in principle both the electrode can be used to read the signal, for pixel detectors, where the number of channel and the complexity of readout are high, only one is actually used. In strip and pad detectors, instead, is more common a dual-side readout

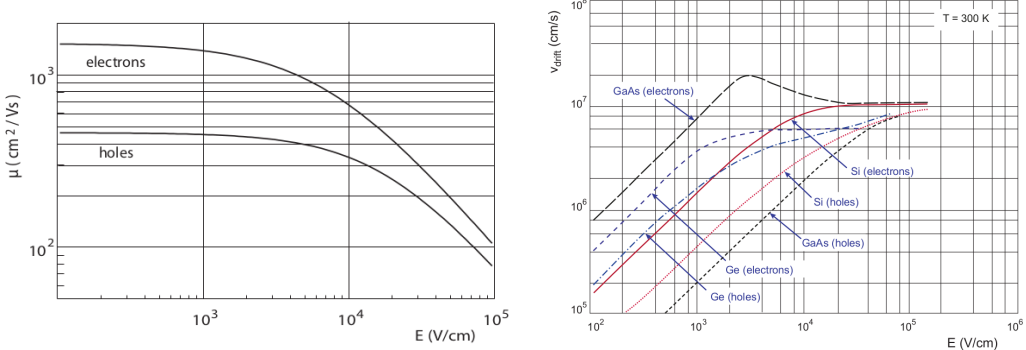


Figure 2.2: (a) Dependence of the mobility on the electric field. (b) Drift velocity at room temperature in different semiconductors

chain is completely sequential and this makes the entire process comparatively slow (tens of ms). A particular type of CCD, the pnCCDs, are typically used to detect low energy (<10 keV) x-ray photons for their homogeneous spatial detection efficiency of photons. The pnCCDs have a sideward depletion similar to silicon drift chambers that makes the electric field stronger, compared with the normal CCDs. The pnCCDs designed for photon imaging are often fabricated with high Z materials, to increase absorption efficacy.

2.3 Hybrid pixels

Hybrid pixels, which currently are the state-of-art technology for large scale pixel detectors in most particle physics experiments, are made of two parts welded together through microconnection (bump bond): the sensor and the electronics (fig. 2.3a). They provide a practical system where the sensor and the ASIC (application specific integrated circuit) can be optimized separately, which makes them really fast, capable of handling with rate up to GHz. However a disadvantage of hybrid pixels is that they must be connected before testing. For reasons related with the historical development, the n⁺-in-n sensors were the first to be used; they demanded double-sided processing which guarantees the detector functionality both before and after the type inversion of the n⁻ doped bulk into p-type after high quantity of radiation. The pn-diode is initially on the unstructured backside of the sensor, while after, the depletion zone grows from the electrode side into the bulk. This ensures that the signal can be sensed on the pixels even if the substrate is no longer fully depleted, even though the bias voltage required for a sufficient depletion increases,

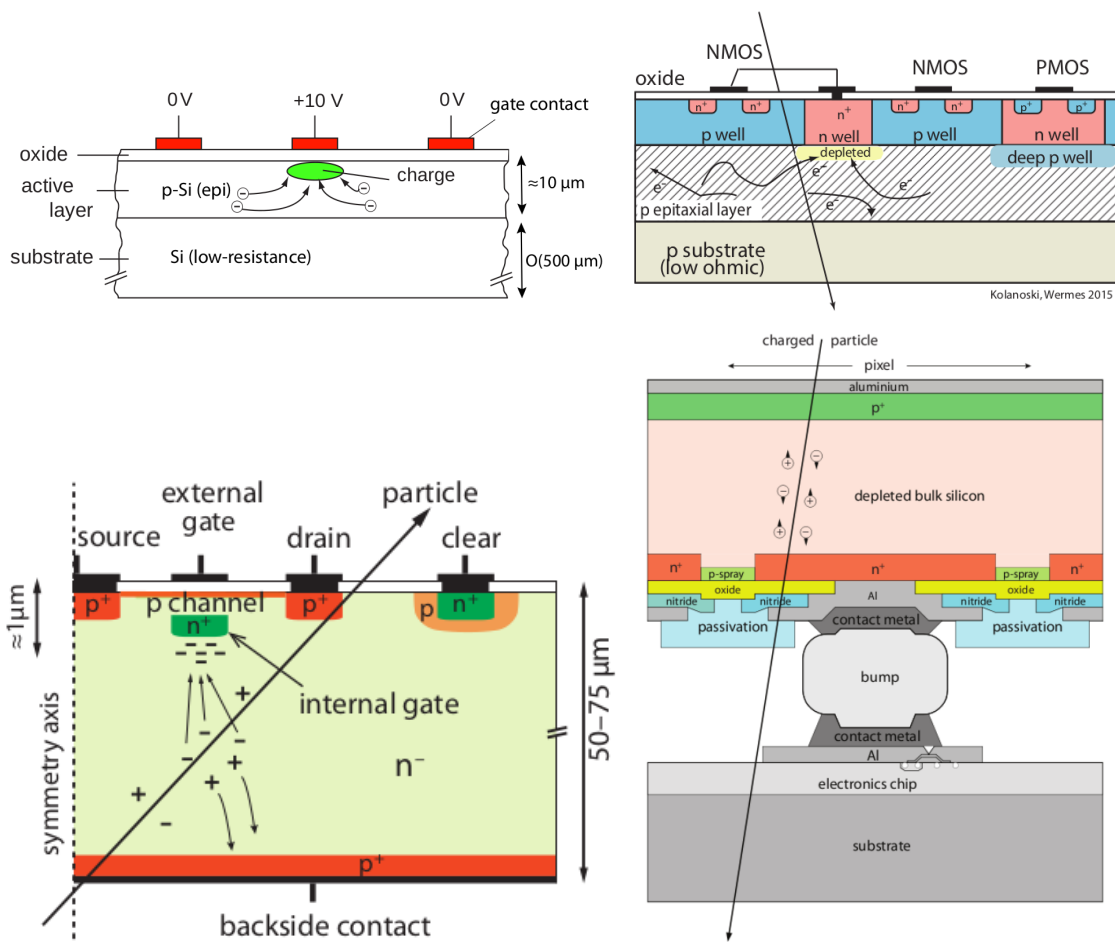


Figure 2.3: Concept cross-section of hybrid pixel (a) and of a DEPFET (b)

193 liming the detector lifetime up to a few years. With the availability of high quality p-
194 substrate material ($\gtrsim 2 \text{ k}\Omega\text{cm}$) the fabrication of n-in-p type sensors, which does not invert
195 anymore, became the preferred choise leading also a huge advance in cost reduction due
196 to no more need of double sided. However, the particular and sophisticated procedure to
197 bond sensor and ASIC makes them difficult to produce, delicate (especially when exposed
198 to high levels of radiation) and also expensive.

199 DEPFET are the first attempt towards the integration of the front end (FE) on the
200 sensor bulk: they are typically mounted on a hybrid structure but the sensor also in-
201 tegrates the first amplification stage. Each pixel implements a MOSFET (metal-oxide-
202 semiconductor field-effect transistor) transistor (a p-channel in fig. 2.3b): a hole current
203 flows from source to drain which is controlled by the external gate and the internal gate
204 together. The internal gate is made by a deep $n+$ implant towards which electrons drift
205 after being created in the depletion region; the accumulation of electrons in the region
206 underneath the n implant changes the gate potential and controls the transistor current;
207 the removal of the signal charge from the internal gate is called "Clear". DEPFET typ-
208 ically have a good S/N ratio: this is principally due to the amplification on-pixel, which
209 guarantees any charge losses, and to the large depletion region. They can be operated in-
210 dividually or integrated in the readout nodes of other detectors, as for example silicon drift
211 chambers, but they always need to be connected to an ASIC with a readout circuit on it.
212 In recent years, the sensor development was driven by an intensive R&D and prototyping
213 for x-ray imagers and the ILC vertex detector.

214 2.4 CMOS MAPS and DMPAS

215 Monolithic active pixels accommodate on the same wafer both the sensor and the FE
216 electronics, with the second one implanted on top within a depth of about $1 \mu\text{m}$ below
217 the surface. MAPS have been first proposed and realized in the 1990s and their practical
218 usage has been enabled by the development of the electronic sector, which guarantees the
219 halving of CMOS transistors dimension at least every two years, as stated by the Moore's
220 law. As a matter of fact the dimension of components, their organization on the pixel
221 area and logic density are important issues for the design and for the layout. Compared

222 to CCDs, the readout time is dramatically reduced by the in-pixel amplification and
223 discrimination, typically followed by a sparsified readout not requiring the signal to be
224 transported anymore over thousands of pixels; as aside effect, the radiation tolerance is
225 also greatly increased by sensing the signal charge directly within its own pixel.

226 A critical parameter for accelerator experiments is the material budget, which repre-
227 sents the main limit factor for momentum measurement resolution in a magnetic field;
228 since hybrid pixels are thicker (\sim hundreds of μm) than monolithic ones (even less than
229 $100 \mu\text{m}$). Using the latter the material budget can be down by a third: typical values for
230 hybrid pixels is 1.5 % X_0 per layer, while for monolithic 0.5 % X_0 . Compared to MAPS,
231 among other disadvantages of hybrid pixels there is the bigger power consumption, that
232 requires also a bigger cooling system, leading to a futher increase of material.

233 Monolithic active pixel can be distinguished between two main categories: MAPS and
234 depleted MAPS (DMAPS). MAPS (figure a ??) have typically an epitaxial layer in a from
235 range $1 \mu\text{m}$ to $20 \mu\text{m}$ and, since they are not depleted, the charge is mainly collected by
236 diffusion rather than by drift. This makes the path of charges created in the bulk longer
237 than usual, making them slow (of order of 100 ns). Moreover, the collection can be partial,
238 especially after irradiation of the detector (look at A for radiation damages), when the
239 trapping probability becomes higher. In figure ?? it is shown as example of CMOS MAPS:
240 the sensor implements an n well as collection diode; to prevent the others n wells (which
241 contain PMOS transistor) of the electronic circuit competing in charge collection and to
242 shield the CMOS circuit from the substrate, additional underlying deep p well are needed.
243 DMAPS are instead MAPS depleted with d typically in $\sim 25 \mu\text{m}$ to $150 \mu\text{m}$ (eq. 2.2) which
244 extends from the diode to the deep p-well, and sometimes also to the backside (in this
245 case if one wants to collect the signal also on this electrode, additional process must be
246 done).

247 2.4.1 DMAPS: large and small fill factor

248 There are two different sensor-design approaches (figure 2.4) to DMAPS:

- 249 • large fill factor: a large collection electrode that is a large deep n-well and that host
250 the embedded electronics

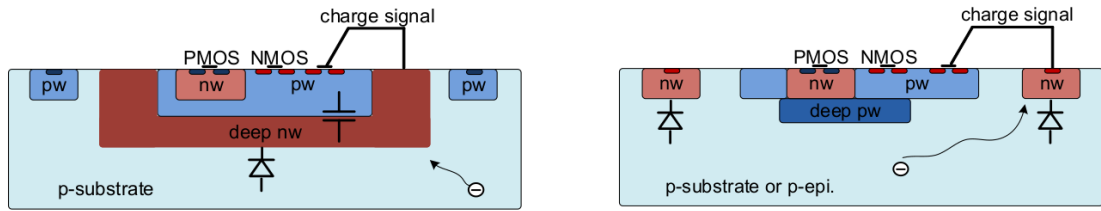


Figure 2.4: Concept cross-section with large and small fill factor

251 • small fill factor: a small n-well is used as charge collection node
 252 To implement a uniform and stronger electric field, DMAPS often uses large electrode
 253 design that requires multiple wells (typically four including deep n and p wells); with this
 254 layout the total capacity of the sensor increases because of the addition of a new term
 255 (fig. 2.5), which contributes to the total amplifier input capacity ($\sim 100 \text{ fF}$). In addition
 256 to the capacity between pixels (C_{pp}) and between the pixel and the backside (C_b), a non-
 257 negligible contribution comes from the capacities between wells (C_{WW} and C_{SW}) needed
 258 to shield the embedded electronics. These capacities affect the thermal and 1/f noise of
 259 the charge amplifier and the τ_{CSA} too:

$$ENC_{thermal}^2 \propto \frac{4}{3} \frac{kT}{g_m} \frac{C_D^2}{\tau_{sh}} \quad \tau_{CSA} \propto \frac{1}{g_m} \frac{C_D}{C_f} \quad (2.5)$$

260 where g_m is the transconductance, τ_{sh} is the shaping time. Among the disadvantages com-
 261 ing from this large input capacity there is a coupling between the sensor and the electronics
 262 resulting in cross talk noise on neighbouring electrodes; indeed, since digital switching in
 263 the FE electronics does a lot of oscillations, this problem is especially connected with the
 intra wells capacities. So, larger charge collection electrode sensors provide a uniform elec-

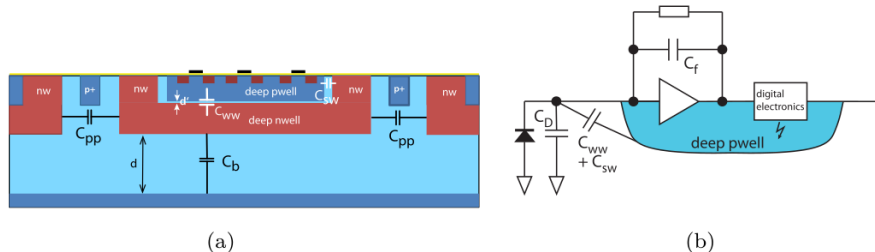


Figure 2.5: C_{pp} , C_b , C_{WW} , C_{SW}

264
 265 tric field in the bulk that results in short drift path and so in good collection properties,

	small fill factor	large fill factor
small sensor C	✓ (< 5 fF)	✗ ($\sim 100\text{--}200\text{fF}$)
low noise	✓	✗
low cross talk	✓	✗
velocity performances	✓	✗ ($\sim 100\text{ ns}$)
short drift paths	✗	✓
radiation hard	✗	✓

Table 2.1: Small and large fill factor DMAPS characteristics

266 especially after irradiation, when trapping probability can become an issue.

267 The small fill-factor variant, instead, benefits from a small capacity (5 fF to 20 fF), but
 268 suffers from a non uniform electric field and from all the issue related to that (slowness
 269 and high trapping probability). As we'll see these two different types of sensor require
 270 different amplifier: the large electrode one is coupled with a charge sensitive amplifier,
 271 while the small one with a voltage amplifier (sec 2.5.1).

272 2.4.2 A modified sensor

273 A process modification, developed by CERN in collaboration with the foundries, which
 274 has become the standard solution to combine the characteristics of a small fill factor
 275 sensor (small input amplifier capacity) and of a large fill factor sensor (uniform electric
 276 field), is the one carried out for ALICE upgrade about ten years [1]. A compromise
 277 between the two sensors could also be making smaller pixels, but this solution requires
 278 reducing the electronic circuit area, so a completely new pixel layout should be though.
 279 The modification consists in inserting a low dose implant under the electrode and one of
 280 its advantage lies in its versatility: in fact, both standard and modified sensor are often
 281 produced for testing.

282 Before the process modification, the depletion region extends below the diode towards
 283 the substrate, and it does not extend much laterally, even if a high bias is applied to the
 284 sensor (fig. 2.6). After the modification, two distinct pn junctions are built: one between

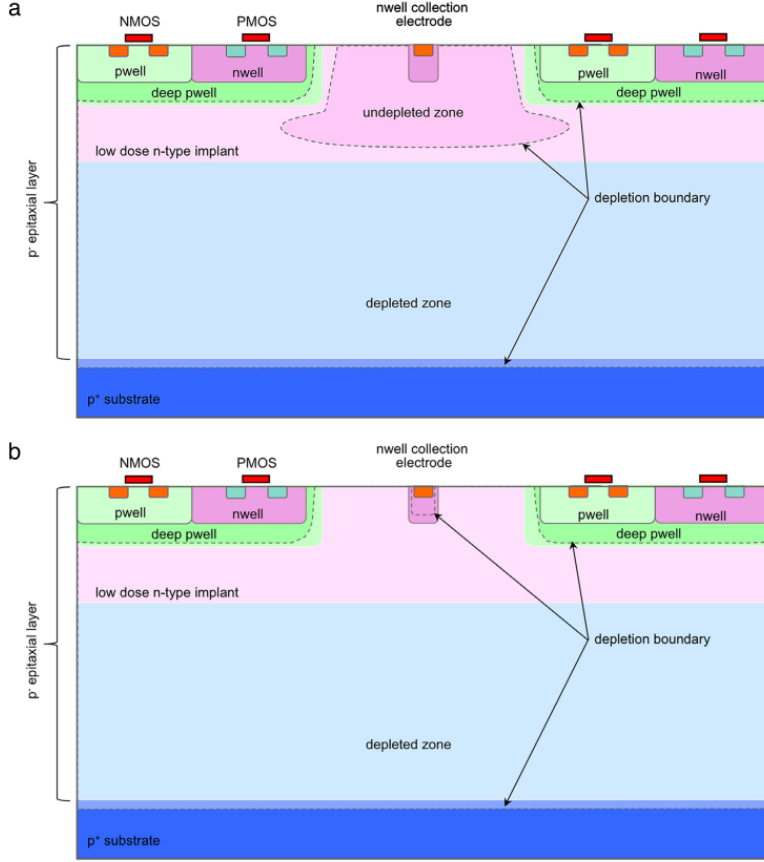


Figure 2.6: A modified process for ALICE tracker detector: a low dose n implant is used to create a planar junction. In (a) the depletion is partial, while in (b) the pixel is fully depleted.

the deep p well and the n^- layer, and the other between the n^- and the p^- epitaxial layer, extending to the whole area of the sensor. Since deep p well and the p-substrate are separated by the depletion region, the two p electrodes can be biased separately² and this is beneficial to enhance the vertical electric field component. The doping concentration is a trimmer parameter: it must be high enough to be greater than in the epitaxial layer in order to prevent the punchthrough between p-well and the substrate, but it must also be low enough to allow the depletion for reasonable bias values.

²This is true in general, but it can be denied if other doping characteristics are implemented, and we will see that this is the case of TJ-Monopix1

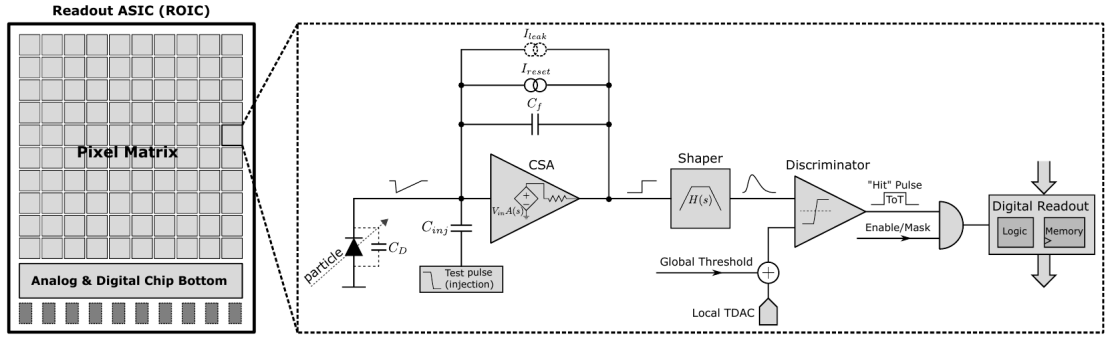


Figure 2.7: Readout FE scheme: in this example the preamplifier is a charge sensitive one (CSA) but changing the capacitive feedback into a resistive one, this can be converted in a voltage or current amplifier.

²⁹² 2.5 Analog front end

²⁹³ After the creation of a signal on the electrode, the signal enters the front end circuit
²⁹⁴ (fig.2.7), ready to be molded and transmitted out of chip. Low noise amplification, fast
²⁹⁵ hit discrimination and an efficient, high-speed readout architecture, consuming as low
²⁹⁶ power as possible, are the goal of the readout integrated electronics (ROIC). The main
²⁹⁷ parts of the analog front end chain are a preamplifier (that often is the only amplification
²⁹⁸ stage) with a reset to the baseline mechanism and a leakage current compensation, a shaper
²⁹⁹ (a band-pass filter) and finally a discriminator. The whole chain must be optimized and
³⁰⁰ tuned to improve the S/N ratio. It is very important both not to have a large noise
³⁰¹ before the amplification stage in order to not multiply that noise, and chose a reasonable
³⁰² threshold of the discriminator to cut noise-hits much as possible.

³⁰³ 2.5.1 Preamplifier

³⁰⁴ Even if circuits on the silicon crystal are only constructed by CMOS, a preamplifier can
³⁰⁵ be processed as an operational amplifier (OpAmp) where the gain is determined by the
³⁰⁶ input and feedback impedance (first step in figure 2.7):

$$G = \frac{v_{out}}{v_{in}} = \frac{Z_f}{Z_{in}} \quad (2.6)$$

³⁰⁷ Depending on whether a capacity or a resistance is used as feedback, respectively a
³⁰⁸ charge or a voltage amplifier is used: if the voltage input signal is large enough and has

309 a sharp rise time, the voltage sensitive preamplifier is preferred. Consequently, this flavor
310 doesn't suit to large fill factor MAPS whose signal is already high enough: $v_{in} = Q/C_D \approx$
311 $3\text{ fC}/100\text{ pF} = 0.03\text{ mV}$, but it's fine for the small fill factor ones: $v_{in} = Q/C_D \approx 3\text{ fC}/3\text{ pF}$
312 $= 1\text{ mV}$.

313 In the case of a resistor feedback, if the signal duration is longer than the discharge
314 time ($\tau = R_S C_D$) of the detector the system works as current amplifier, as the signal
315 is immediately transmitted to the amplifier; in the complementary case (signal duration
316 longer than the discharge time) the system integrates the current on the C_D and operates
317 as a voltage amplifier.

318 2.6 Readout logic

319 The readout logic includes the part of the circuit which takes the FE output signal, pro-
320 cesses it and then transmit it out of pixel and/or out of chip; depending on the situation
321 of usage different readout characteristics must be provided. To store the analogical in-
322 formation (i.e. charge collected, evolution of signal in time, ...) big buffers and a large
323 bandwidth are needed; the problem that doesn't occur, or better occur only with really
324 high rate, if one wants record only digital data (if one pixel is hit 1 is recorded, and if not
325 0 is recorded).

326 A common compromise is to store the time over threshold (ToT) of the pulse in clock
327 cycle counts; this needs of relatively coarse requirement as the ToT can be trimmed down
328 to use only a dozen bits but, being correlated (and hopefully linear) with the deposited
329 charge, it provides a sufficient information. The ToT digitalization usually takes advantage
330 of the distribution of a clock (namely BCID, bunch crossing identification) on the pixels'
331 matrix. The required timing precision is better than $\sim 25\text{ ns}$, that corresponds to the period
332 between bunch collisions at LHC; for such reason a reasonable BCID-clock frequency for
333 pixels detector is 40 MHz .

334 Moreover, the readout architecture can be full, if every hit is read, or triggered, if a
335 trigger system decides if the hit must be stored or not. On one hand the triggered-readout
336 needs buffers and storage memories, on the other the full readout, because there is no
337 need to store hit data on chip, needs an high enough bandwidth. A triggered readout is

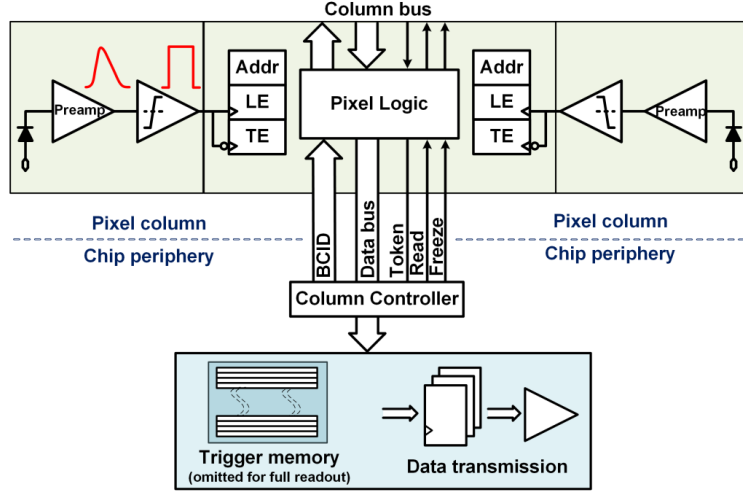


Figure 2.8: Column drain R/O scheme where ToT is saved

fundamental in accelerator experiments where the quantity of data to store is very large and some selection has to be applied by the trigger: to give an order of magnitude, at LHC more than 100 TBit/s of data are produced, but the storage limit is about 100 MBit/s [2](pag. 797). Typically, the trigger signal is processed in a few μs , so the pixel gets it only after a hundred clock cycles from the hit arrival time: the buffer depth must be able to handle such high trigger latency.

After having taken out the data from the pixel, it has to be transmitted to the end of column (EoC) where a serializer delivers it out of chip, typically to an FPGA. There are several ways of transmitting data from a pixel to the EoC: one of the most famous is the column-drain read out, developed for CMS and ATLAS experiments [3]. All the pixels in a double-column share a data bus and only one pixel at a time, according to a priority chain, can be read. The reading order circuit is implemented by shift register (SR): when a hit arrives, the corresponding data, which can be made of timestamp and ToT, is temporarily stored on a RAM until the SR allows the access to memory by data bus. Even if many readout architectures are based on the column-drain one, it doesn't suit for large size matrices. The problem is the increasing number of pixels on a column would also raise the number of pixels in the priority chain, which would result in a slowdown of the readout.

If there isn't any storage memory, the double-column behaves as a single server queue and the probability for a pixel of waiting a time T greater than t , with an input hit rate

358 on the column μ and an output bandwidth B_W is [4]:

$$P(T > t) = \frac{\mu}{B_W} e^{-(B_W - \mu)t} \quad (2.7)$$

359 To avoid hit loss (let's neglect the contribution to the inefficiency of the dead time τ due
 360 to the AFE), for example imposing $P_T > t \sim 0.001$, one obtains $(B_W - \mu) t_t \sim 6$, where
 361 t_t is the time needed to transfer the hit; since t_t is small, one must have $B_W \gg \mu$, that
 means a high bandwidth [4].

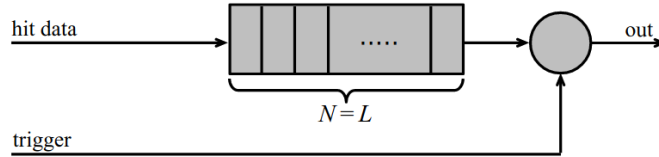


Figure 2.9: Block diagram of a pipeline buffer: N is the dimension of memory buffer and L is the trigger latency expressed in BCID cycles

362

363 Eq.2.7 is actually an approximation, since each pixel sees a different bandwidth de-
 364 pending on the position on the queue: the first one sees the full bandwidth, while the next
 365 sees a smaller one because it can be occasionally blocked by the previous pixel. Then,
 366 the bandwidth seen by the pixel i is $B_i = B - \sum_j \mu_j$, where μ_j is the hit rate of the j th
 367 pixel. The efficiency requirement on the bandwidth and the hit rate becomes: $B_{W,i} > \mu_i$,
 368 where the index i means that the constraint is for a single pixel; if all the N pixels on a
 369 column have the same rate $\mu = N\mu_i$, the condition reduces to $B_W > \mu$. The bandwidth
 370 must be chosen such that the mean time between hits of the last pixel in the readout chain
 371 is bigger than that. In order to reduce the bandwidth, a readout with zero suppression
 372 on pixel is typically employed; this means that only information from channels where the
 373 signal exceeds the discriminator threshold are stored.

374 If, instead, the signal is locally stored until a trigger signal arrives, the input rate to
 375 column bus μ' is reduced compared to the hit rate μ as: $\mu' = \mu \times r \times t$, where r is the
 376 trigger rate and t is the bunch crossing period. In this situation there is a more relaxed
 377 constraint on the bandwidth, but the limiting factor is the buffer depth: the amount of
 378 memory designed depends both on the expected rate μ and on the trigger latency t as
 379 $\propto \mu \times t$, which means that the higher the trigger latency the lower the hit rate to cope
 380 with.

381 In order to have an efficient usage of memory on pixels' area it's convenient grouping
 382 pixels into regions with shared storage. Let's compare two different situations: in the first
 383 one a buffer is located on each pixel area, while in the second one a core of four pixels
 384 share a common buffer (this architecture is commonly called FE-I4).

Consider a 50 kHz single pixel hits rate and a trigger latency of 5 μs , the probability of

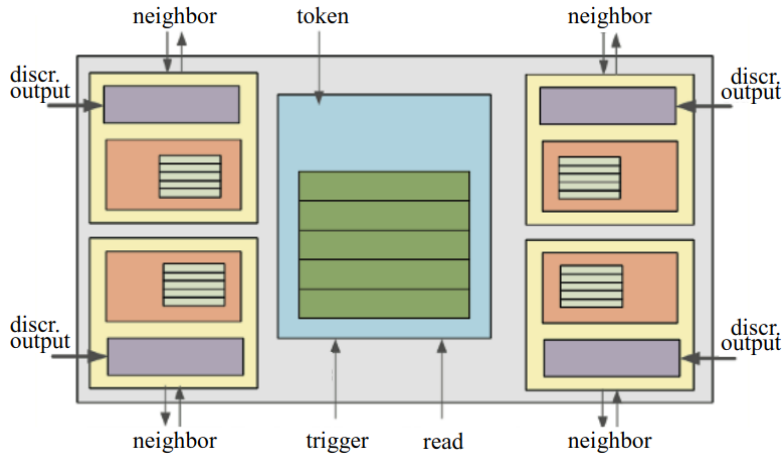


Figure 2.10: Block diagram of the FE-I4 R/O. Read and memory management section is highlighted in light blue; latency counters and trigger management section are highlighted in green; hit processing blocks are highlighted in purple; ToT counters and ToT management units are highlighted in orange

385

386 losing hits is:

$$P(N > 1|\nu) = 1 - P(N = 0|\nu) - P(N = 1|\nu) = 1 - e^{-\nu}(1 + \nu) \approx 2.6\% \quad (2.8)$$

387 where I have assumed a Poissonian distribution with mean $\nu = 0.25$ to describe the counts

388 N.

389 To get an efficiency ϵ greater than 99.9 % a 3 hit depth buffer is needed:

$$P(N > 3|\nu) = 1 - \sum_{i=0}^3 P(N = i|\nu) < 0.1\% \quad (2.9)$$

390 Consider the second situation: if the average single pixel rate is still 50 kHz, grouping four
 391 pixels the mean number of hits per trigger latency is $\nu = 0.25 \times 4 = 1$. To get an efficiency
 392 of 99.9% (eq. 2.9) a buffer depth of 5 hits in the four-pixels region, instead of 3 per pixels,
 393 is needed.

394 **Chapter 3**

395 **Use of pixel detectors**

396 There always was a tight relation between the development of cameras and pixel detec-
397 tors since 1969, when the idea of CCDs, thanks to whom Boyle and Smith were awarded
398 the Nobel Prize in Physics in 2009, revolutionized photography allowing light to be cap-
399 tured electronically instead of on film. Even though the CMOS technology was already
400 known when CCDs spread, the costs of productions were too high to allow the diffu-
401 sion of these sensors for which would take almost 20 years. From that period on, the
402 fast diffusion of CMOS was mainly due to the less cost than CCD, and the less power
403 supply required. Nowadays CCDs are still preferred over MAPS in astronomy, where the
404 astronomical sources' rate are low enough to cope with slow readout time (tens of ms).

405 The principal use cases of pixel detectors are particle tracking and imaging: in the
406 former case individual charged particles have to be identified, in the latter instead an
407 image is obtained by the usually un-triggered accumulation of the impinging radiation.
408 Also the demands on detectors performance depends on their usage, in particular tracking
409 requires high spatial resolution, fast readout and radiation hardness.

410 **3.1 Tracking in HEP**

411 At first the physics world overlooked the CCDs, and all pixel in general, as against the
412 gaseous detector for tracking: there was no need to replace these ones which had a sufficient
413 good resolution ($100\text{ }\mu\text{m}$). Since 1974, with the measurement of the invariant mass of the
414 J/Psi and the affirmation of the quark model, all experiments start to look for better

415 spatial resolutions in order to achieve the possibility of reconstructing short lived particle.

416 Historically, the first pixel detector employed in particle physics was a CCD: it was
417 installed in the spectrometer at the CERN's Super Proton Synchrotron (SPS) by the
418 ACCMOR Collaboration (Amsterdam, CERN, Cracow, Munich, Oxford, RAL) at mid
419 1980s, with the purpose of studying the (at the time) recently-discovered charm particles.
420 The second famous usage of CCDs took place at SLAC in the Large Detector (SLD) during
421 the two years 1996-98, where the CCD technology was adopted instead of the microstrip
422 detectors for their excellent spatial resolution (cell size $22\text{times}22\mu\text{m}^2$ giving a resolution of
423 $\sim 5\mu\text{m}$) thanks to the sufficient time for readout between two successive collisions (160 ms).

424 From that period on particle tracking in experiments have been transformed radically:
425 it was mandatory for HEP experiments to build an inner vertex detector, where the general
426 tasks are:

- 427 • pattern recognition with the identification of particle tracks at large backgrounds and
428 pile-up
- 429 • measurement of vertices (primary and secondary)
- 430 • multi-track and vertex separation in the core of jets
- 431 • measurement of specific ionization
- 432 • momentum measurement combining with other detectors informations

433 In 1991, the more demanding environments led to the development of hybrid pixel
434 detectors: a dedicated collaboration, RD19, was established at CERN with the specific goal
435 of defining a semiconductor micropattern detector with an incorporated signal processing
436 at a microscopic level. In those years a wide set of prototypes of hybrid pixel has been
437 manufactured; among the greatest productions a mention goes to the huge ATLAS and
438 CMS vertex detectors. From the middle of 2013 a second collaboration, RD53, has been
439 established with the new goal of finding a pixel detector suitable for phase II future
440 upgrades of those experiments. Even if the collaboration is specifically focused on design
441 of hybrid pixel readout chips (aiming to 65 nm technique so that the electronics fits within
442 the pixel area), also other options have been taken in account and many tests have been done

443 on MAPS. Requirements imposed by HL-LHC will become tigher in time: for example, a
444 dose and radiation of 5 Mrad and 10^{16} NIEL are exepcted after 5 years of operation. Time
445 resolution, material budget and power consumption are also issues for the upgrade: to
446 distinguish different events from different bunches a time resolution better than 25 ns for
447 a bunch crossing frequency of 40 MHz is required, and also a material budget lower than
448 2% and a power consunption lower than 500 mW/cm² are required.

449 Amidst the solutions proposed 3D silicon detector, invented by Sherwood Parker in
450 1995, and MAPS are the most promising. In 3D sensors the electrode is a narrow column
451 of n-type implanted vertically across the bulk instead of being implanted on the wafer's
452 surface. The charge produced by the impinging particle is then drifted transversally within
453 the pixel, and, as the mean path between two electrode can be soufficent low, the trap
454 probability is not an issue. Even if 3D detector are adequately radiation hard and are a
455 strong contender for hybrid pixel modules, especially in the innermost pixel detector layer,
456 the fabrication process is currently low volume, making them unlikely to cover large areas.

457 3.1.1 Hybrid pixels at LHC and at SuperKEKB

458 ATLAS

459 With CMS, ATLAS is one of two general-purpose detectors at the LHC and has the largest
460 volume detector ever constructed for a particle collider (46 m long and 25 m in diameter).
461 The Inner Tracker (ITk) consists of three different systems all immersed in a magnetic
462 field parallel to the beam axis whose main components are: the pixel, the micro-strips and
463 transition radiation trackers. Concerning the pixel detector, they installed a 3-layer hybrid
464 pixel detector in 2007 and an additional one inserted within the original detector envelope
465 and therefore called insertable B-layer (IBL) in 2014. 92 million pixels are divided in 4
466 barrel layers and 3 disks in each end-cap region, covering a total area of 1.9 m² and having
467 a 15 kW of power consumption.

468 As stated by the ATLAS collaboration the pixel detector is exposed by an extreme
469 particle flux: "By the end of Run 3¹, the number of particles that will have hit the
470 innermost pixel layers will be comparable to the number it would receive if it were placed

¹Run 3 start in June 2022

only a few kilometres from the Sun during a solar flare". Considering that the particle density will increase even more with HL-LHC, radiation hardness is definitively target to achieve. The most ambitious goal is employ a MAPS-based detector for the inner-layer barrels, and for this reason the RD53 collaboration is designing many MAPS prototypes (as for example TJ-Monopix1, which I will talk about in chapter 4) and performing test. Up to now this possibility will be eventually implemented during the second phase of the HL-LHC era, as at the start of high-luminosity operation the selected option is the hybrid one. The sensor will be bonded with ITkPix, the first full-scale 65 nm hybrid pixel-readout chip developed by the RD53 collaboration. Regarding the sensor, a valuable option is using 3D pixels, which have already proved themselves in ATLAS, for the IBL, where they were introduced in a limited acceptance range and introduced a new readout integrated circuit called FE-I4. Also the complexity of the readout will be raised, as the number of pixels will be increased of a factor about 7, passing from 92 millions to 6 billion.

484 CMS

485 The CMS hybrid pixel detector has been upgraded in 2017, when, with the replacement
486 of a piece of the beam pipe, a layer has been added to the detector at 3 cm from it.
487 124 million pixels are divided between the barrel pixel detector (BPIX) and the forward
488 disks (FPIX), with sensors which are different from each other and produced by different
489 foundries. The sensors have an area equal to 100 μm by 150 μm and have been produced
490 on 285 μm to 300 μm thick wafers.

491 The time resolution is 25 ns, and the information coming from the detector are stored on
492 chip for the Level-1 trigger latency ($\sim 4 \mu\text{s}$). The upgrade baseline ROIC was redesigned for
493 the outer 3 layers, replacing analog signal readout with on-chip ADCs and digital readout
494 at higher rate. reads out the pulse height information for each pixel.

495 LHCb

496 LHCb is a dedicated heavy-flavour physics experiment that exploits pp interactions at
497 14 TeV at LHC. It was the last experiment to upgrade the vertex detector, the Vertex
498 Locator (VELO), replacing the silicon-strip with 26 plane pixel detector (because of the
499 fixed target geometry) in May 2022. As the instantaneous luminosity in Run3 is increased

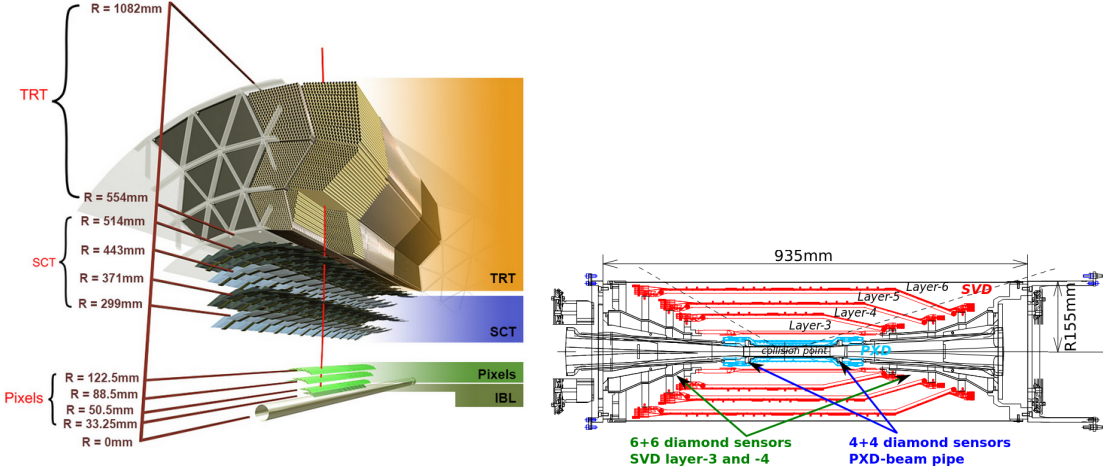


Figure 3.1: (a), (b) Since an accidental beam background enhancement can damage the VXO, diamond detectors are installed in order to monitor it.

500 by a factor $\lesssim 10$, much of the readout electronics and of the trigger system have been
 501 developed in order to cope with the large interaction rate. To place the detector as close as
 502 possible to the beampipe and reach a better track reconstruction efficiency and resolution,
 503 the VELO has a surprising feature: during the injection of LHC protons it is parked at
 504 3 cm from the beams and only when the stability is reached it is moved at ~ 5 mm. Readout
 505 speed is a priority for the detector that uses a triggerless readout at 40 MHz collision rate,
 506 producing 20 Gbps per ROIC. The Velopix, which is the hybrid system designed for LHCb,
 507 is made bonding sensors, each measuring 55×55 micrometers, 200 μm -thick to a 200 μm -
 508 thick ASIC specially developed for LHCb and coming from the Medipix family (sec. ??),
 509 which can handle hit rates up to 900 MHz per chip. Since the detector is operated under
 510 vacuum near the beam pipe, the heat removal is particularly difficult and evaporative CO₂
 511 microchannel cooling are used.

512 **BelleII**

513 Due to the high background level coming from the nanobeam used at SuperKEKB in order
 514 to achieve a such high luminosity ($4.7 \times 10^{34} \text{ cm}^{-2}/\text{s}$), silicon strip cannot be used in the
 515 inner layer of the tracker. The occupancy is too high to allow the usage of strips up to
 516 40 mm from the beam pipe. Moreover for a precise reconstruction of B-decay vertices, the
 517 usage of thin detector is mandatory at the low energy (4 GeV to 7 GeV) of the beam, in

518 order to minimize the multiple scattering of particles.

519 The current vertex detector of BelleII, VXD, is made of a pixel detector (PXD), fab-
520 ricated with 2 layers of DEPFET-based pixels, and 4 layers of a double-sided silicon strip
521 detectors (SVD)[5]. Due to the small capacitance of the collection node, DEPFET presents
522 a high signal-to-noise ratio (in 30-50) thanks to the low intrinsic noise and to the large
523 signal achieved with the fully depleted bulk: pixels are thinned to 75 μm in the active
524 region, then a MIP is supposed to create a signal of $\sim 6000 \text{ e}^-$, while the typical noise of
525 DEPFET is around 200 e^- . The ASIC read out is still based on a rolling shutter logic,
526 with an integration time of 20 μs . In order to reduce the data-storage memory PXD hits
527 are only used to improve spatial resolution of tracks: the SVD informations are used by
528 the High Level Trigger (HLT) to look for regions of interest in the pixel ladders just by
529 extrapolating back the tracks found in the tracker detector, and this method allows to
530 store only data belonging to these areas; the PXD hits are then used in offline track fit to
531 improve the vertex resolution.

532 MAPS have been proposed for the replacement of VXD during the Long Shut Down
533 2 (LSD2) foreseen around 2026-27; the new vertex detector, VTX, should be made of 5
534 layers fabricated by the optimized Belle II pixel sensor (OBELIX), a detector based on
535 TJ-Monopix have been selected (look at chapter ??). The main advantages VTX should
536 bring are a obvious improving in the track and vertex resolution ($14 \mu\text{m}$ before upgrade,
537 $\lesssim 10 \mu\text{m}$ expected after upgrade) and a reduction in the X_0 (da.. a..), a higher background
538 tolerance because of the smaller sensor than strips dimension and a low bandwidth due to
539 the on-chip sparsification.

540 3.1.2 First attempts to MAPS

541 MIMOSA at EUDET and STAR

542 MIMOSA [6][7] (standing for Minimum Ionizing MOS Active pixel sensor), designed in
543 2008, prefigured the architecture of MAPS for coming vertex detector being the first large
544 scale sensor to be employed as detector. MIMOSA-26 equiped the final version of EUDET
545 high resolution beam telescope both at CERN-SPS and at DESY while the MIMOSA-
546 28 devices are used for the first MAPS-based vertex detector at the STAR experiment.



Figure 3.2: (a) The HFT PXL detector; (b) Block-diagram of the ULTIMATE-2 sensor

547 MIMOSA-26 is fabricated in a 350 nm, and a module features 1152 columns, split into
 548 18 independent groups, and 576 rows, with square pixels having a side of 18.4 μm length;
 549 the epitaxial layer is not fully depleted and the charge collection is mostly by diffusion,
 550 resulting in charge sharing between pixels and collection time bigger than 100 ns.

551 The readout is done in a rolling shutter mode and it is the first MAPS integrating on
 552 chip the zero suppression: the chip is an Active Pixels (APS) and therefore it incorporates
 553 the amplification on pixel, while the signal discrimination and zero-suppression logic are
 554 placed at the EoC, where is also placed a memory. The chip is an Active Pixels (APS)
 555 and therefore it incorporates the amplification on pixel, while the signal discrimination
 556 and zero-suppression logic are placed at the EoC: the readout is done in a rolling shutter
 557 mode with a frame integration time that can be lowered down to 85 ms, and a memory
 558 allowing to store up to six hits is.

559 The EUDET telescope, equipped with six sensor planes, requires highly granular and
 560 thin pixel detectors in order to achieve an excellent track resolution (around 2 μm) even at
 561 the rather low particle energies of up to 6 GeV. The STAR experiment at the Relativistic
 562 Heavy Ion Collide (RHIC) accelerator at the Brookhaven National Laboratory (BNL) is
 563 the first to include MAPS in the vertex detector[8]. The main tracking detector in STAR is
 564 a TPC with radii 60-190 cm embedded in a 0.5 T solenoidal magnetic field, that provides
 565 a pointing resolution of approximately 1 mm. The pixel detector, PXL, is a part of a

566 3-detector system, Heavy Flavor Tracker (HFT), that has been added to the pre-existing
 567 STAR apparatus just before the 2014 Run in order to improve the impact parameter
 568 resolution and to enable the direct reconstruction of hadronic decays of heavy flavor mesons
 569 and baryons. The Heavy Flavor Tracker (HFT) is composed by the Silicon Strip Detector
 570 (SSD), the Intermediate Silicon Tracker (IST) and the Pixel Detector (PXL); the first
 571 one is placed at 22 cm from the beam pipe and consists of double sided strips with 95 μm
 572 inter-strip pitch, the second one, placed at 14 cm, is made of single sided silicon pads
 573 with $600 \mu\text{m} \times 6 \text{ mm}$ pitch and the last one made by two layers is placed at 2.8 cm and 8 cm
 574 fabricated with ULTIMATE2 (also known as MIMOSA-28), a successor of MIMOSA-26
 575 sensor, with pitch 20.7 μm and thinned down to 50 μm . An area of 0.16 m^2 are covered
 576 by 400 MAPS sensor, corresponding to 356 millions of pixels divided into array size of 928
 577 \times 960. Each pixel includes circuitry for readout, amplification, and Correlated Double
 578 Sampling (CDS) for signal extraction and noise subtraction and the frame integration time
 579 is 185.6 μs ; after the subtraction the signal to noise ratio is ~ 30 , with a noise between
 580 10-12 electrons and a signal of $1000 e^-$. Thanks to the HFT system and the PXL, STAR
 581 achieved a track pointing resolution 46 μm for $750 \text{ MeV}/c$ kaons, and better than 30 μm for
 582 particle momenta bigger than $1 \text{ GeV}/c$: this performance enabled the study of D-meson
 583 production with a high significance signal.

584 **ALPIDE at ALICE**

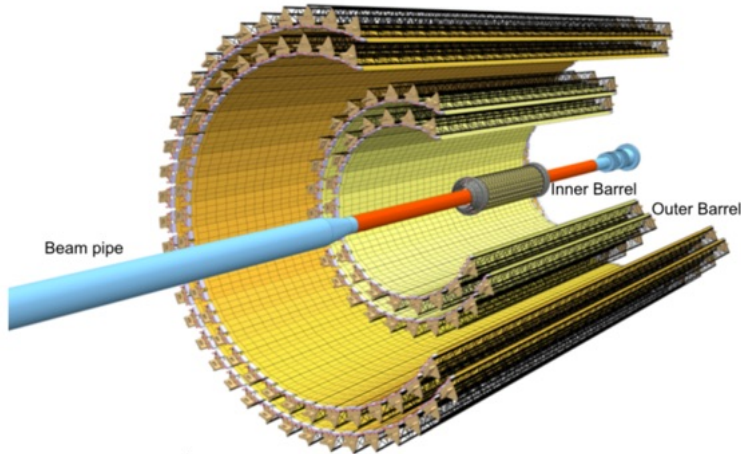


Figure 3.3

585 ALICE (A Large Ion Collider Experiment) is a detector dedicated to heavy-ion physics
586 at the LHC. The tracking detector consists of the Inner Tracking System (ITS), the gaseous
587 Time Projection Chamber (TPC) and the Transition Radiation Detector (TRD), and all
588 those are embedded in a magnetic field of 0.5 T. The ITS is made by six layers of detectors,
589 two for each type, from the interaction point outwards: Silicon Pixel Detector (SPD),
590 Silicon Drift Detector (SDD) and Silicon Strip Detector (SSD). Contrary to the others
591 LHC experiments, ALICE tracker is placed in a quite different environments: the expected
592 dose is smaller by two order of magnitude and the rate of interactions is few MHz instead
593 of 40 MHz, but the number of particles comes out of each interaction is higher (the SPS is
594 invested by a density of particles of $\sim 100 \text{ cm}^{-2}$). The reconstruction of very complicated
595 events with a large number of particle is a challenge, hence to segment and to minimize
596 the amount of material, which may cause secondary interaction complicating further the
597 event topology, is considered a viable strategy.

598 ITS2, upgraded during the LHC long shut down in 2019-20, was the first large-area
599 ($\sim 10 \text{ m}^2$ covered by 2.5 Gpixels) silicon vertex detector based on CMOS MAPS. The
600 detector employs the ALPIDE chip, developed by ALICE collaboration, fabricated in the
601 180 nm CMOS Imaging Sensor process of TowerJazz, whose design takes full advantage
602 of process feature which allows full circuitry within the pixel matrix. Thanks to the
603 reduction of the material budget, ITS2 obtained an amazing improvement both in the
604 position measurement and in the momentum resolution, improving the efficiency of track
605 reconstruction for particle with very low transverse momentum (by a factor 6 at $pT \sim$
606 0.1 GeV/c). Further advancements in CMOS MAPS technology are being aggressively
607 pursued for the ALICE ITS3 vertex detector upgrades (foreseen around 2026-27), with
608 the goals of further reducing the sensor thickness and improving the readout speed (which
609 now is completely asynchronous) of the devices, while keeping power consumption at a
610 minimum.

611 3.2 Other applications

612 Historically for imaging purpose the CCDs were the favoured device: they can be used as
613 single photon counter or integrating and collecting the charge released by more impinging

614 particles. The utilisation in the first case is similar to the tracking one, except that the
615 requirements are less tight, so much that two noteworthy of microchips originally meant
616 for detectors in particle physics at the LHC, and later employed in other fields are Medipix
617 and Timepix. They are read-out chips developed by the Medipix Collaborations since early
618 1990s. For two decades, different Medipix generations have been produced, having a rough
619 correlation with the feature size used: Medipix2 (1999) used 250 nm feature size CMOS
620 while Medipix3 (2005) 130 nm. For photons imaging other materials with higher atomic
621 charge than silicon could be preferred, as a high photon absorption efficiency is needed: it
622 was for this reason that Medipix2 was bump bonded to identically segmented sensors of
623 both silicon and GaAs.

624 The applications in scientific imaging vary from astrophysics and medical imaging and
625 dosimetry to more exotic domains as studies of protein dynamics, material science, art
626 authentication and archaeology. One of the most important employment of Medipix is as
627 X-ray single photon counting in industrial and medical radiography and in 3D computed
628 tomography². Thanks to a New-Zealand company, the MARS Bioimaging detector has
629 been fabricated, which is capable of resolving the photons energy and produce 3D coloured
630 images. Besides tracking in HEP (I have already cited the use of Timepix3 is in the beam
631 telescope of the LHCb VELO), an important use of Timepix is in dosimetry. **Timepix**
632 **Detector for Imaging in Ion Beam Radiotherapy- articolo e qualche info.** A small-Timepix
633 detector with the dimension of a USB can also be found at the International Space Station,
634 where it is exploited for radiation, principally made of heavy-ion, monitoring.

635 3.2.1 Applicability to FLASH radiotherapy

636 A possible new application of pixels detector is dosimetry or beam monitoring of charge
637 particles in high intensity radiography. Recently³ a promising method for RT at ultra high
638 dose rate (at least 40 Gy/s) and for this reason called FLASH-RT[9], instead of CONV-RT
639 (0.03 Gy/s), came out. However, finding dosimeters suitable at ultra high dose rate is still

²The analysis of the direction dependence of X-ray absorption is performed, for example, in order to obtain an image in Computed Tomography (CT)

³The first evidences has been observed on a mice experiments in 1966 and in 2014 by the group of Favaudon and Vozenin. After this, many test on cats and pigs have been performed, and also there has been a clinical trial on a cutaneous tumor-patient

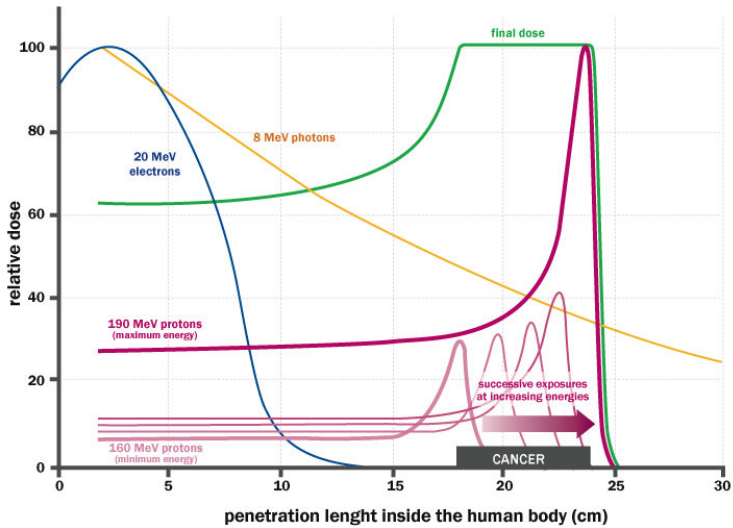


Figure 3.4: The Spread Out Bragg Peak (SOBP) curve (green), which is a constant dose distribution, is obtained from the superposition of many Bragg peak of hadrons with different energy.

640 an open issue since almost all standard online dosimeters have shown saturation problems.

641 Radiotherapy

642 The radiological treatment is a common method used in 60% of tumors both as palliative
 643 care and as treatment. It can be given before, after or during a surgery, (Intra opera-
 644 tive radiation therapy-IORT) and many different types of radiations (photons, electrons,
 645 protons and ions, which mainly are hydrogen and carbon) can be used to irradiate the
 646 affected tissues. Exploiting the ionizing energy loss, that can be parametrized by the
 647 Linear Energy Transfer (LET), a biological damage can be delivered to the tissue: while α
 648 and β particles are high LET radiations with values in $100 \text{ keV}/\mu\text{m}$ to $200 \text{ keV}/\mu\text{m}$, x-rays
 649 and gamma-rays are low LET radiations with values in range $0.2 \text{ keV}/\mu\text{m}$ to $2 \text{ keV}/\mu\text{m}$. If
 650 x-ray photons, with energy in 4 MeV to 25 MeV are used, the ionization is caused by the
 651 Compton electrons and is more in the superficial layers of the tissue due to the exponen-
 652 tial attenuation of the beam. The hardrons energy loss, instead, is strongly localized in
 653 the last region of the track, that is the Bragg peak, such as the the treatement typically
 654 requires the scanning of the target. The Relative Biological Effectiveness (RBE) of ions

	CONV-RT	FLASH-RT
Dose rate	0.03 Gy/s	40 Gy/s
Intra pulse dose rate	100 Gy/s	106 Gy/s
Treatment duration	~minutes	\lesssim 500 ms
Dose Per Pulse	0.3 mGy	1 Gy to 10 Gy
Pulse width	3 μ s	\sim 2 μ s

Table 3.1: Typical value of treatment parameters

655 near th Bragg peak depends on their mass, and in particular it increases with the ion's
 656 mass; even though, too heavy ions generally increases the damage produced also in the
 657 entrance region. Carbon is considered the optimum between the two trends.

658 Electrons, instead, of energy in range of a dozen of MeV tend to spread out on a
 659 bigger region of a few centimeters in both the diameter and thickness. Using Very High
 660 Energy Electrons (VHEE) has been taken into account for irradiation of deeper tissues,
 661 however, to date, the FLASH effect has been tested and demonstrated only using low-energy
 662 electrons.

663 **FLASH effect**

664 This treatment takes advantages of biological differences between tumors and healthy
 665 tissues: it is characterized by reducing normal tissue toxicity and maintaining equivalent
 666 tumor damage. The response to dose can be described by the survival fraction probability,
 667 describing the fraction of surviving cell as a function of the dose:

$$S(D) = S(0) e^{-(\alpha D + \beta D^2)} \quad (3.1)$$

668 where α and β respectively represents the rate of cell killing by single ionizing events and
 669 by double hits. Hence, at high doses the density of damages increases and the cells repair
 670 becomes more difficult. Even if the FLASH effect is not yet completely understood and
 671 the underlying mechanisms are not clear, it looks like there are two different recipes which
 672 are involved:

- 673 • **The dose rate:** higher dose rate produce bigger damages (fig. 3.5(a)) since this

674 prevent cells from sparing.

- 675 • **The presence or absence of oxygen:** while hypoxic cells are very resistant to radi-
676 ation, normal oxygenated cells are highly radiosensitive. This is because if molecules
677 containing O_2 break due to the impinging radiation, then the oxygen can build Re-
678 active Oxygen Species (ROS) (fig.3.5(b))

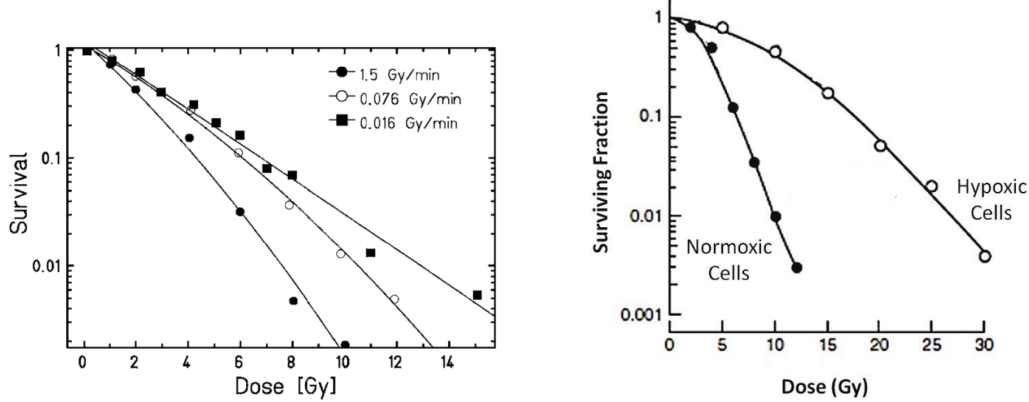


Figure 3.5: (a) Survival curve for different dose rate and (b) for different oxygen cell content

679 The Tumor Control Probability (TCP) and the Normal Tissue Complication (NTC)
680 functions parametrize respectively the efficiency of damaging on the tumor after having released
681 a certain dose and the probability of not affecting the healthy tissues. The intermediate
682 zone between the increase of the TC and of the NTC is called therapeutic window, and
683 the wider it is and the more effective the treatment is.

684 Dosimetric problems

685 Up to now, all online dosimeters have shown saturation problems at high DDP, differently
686 from radiochromic films, which are the standard passive dosimeters and have shown a
687 dose-rate independence up to 109 Gy/s. Even though the linear response in wide dynamic
688 range, they do not provide any online dosimetric informations, since the time required to
689 extract the physical value from the reading is not instantaneous⁴.

690 Ionization Chambers (ICs), which are the online reference dosimeter also according to
691 law, at high level of radiation (already at dose per pulse two orders of magnitude lower

⁴COSA sono e più o meno come funzionano

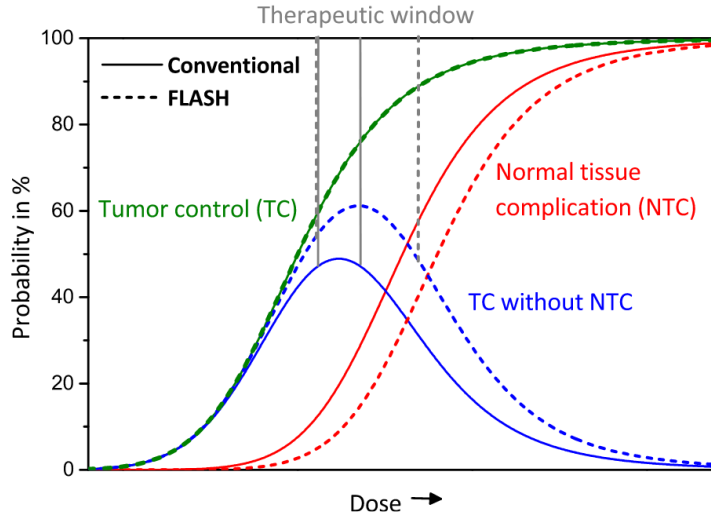


Figure 3.6: Illustration of dependence of TCP, NTCP and therapeutic window on dose, for CONV-RT ad FLASH-RT.

than the ones used for FLASH-RT) show both problems of saturation and recombination. When a high density of ions and electrons is produced in the gas, a high counter electric field opposed to the drift one might be generated; if a neutral region build up, both the recombination of i/e pairs, with a subsequent photoemission and abrupt discharge can happen⁵. For low level of radiation a correction factors, k_{sat} , can be introduced and a dose measurement can still be done: with Dose Per Pulse (DDP) lower than 1 mGy the correction factor is <5%. Non sono sicurissima di aver capito davvero il punto per quanto riguarda i semiconduttori e gli scintillatori

In reference [10] are presented some results related with saturation problems at high DDP of different types of detectors. The dosimeters tested and their value at which saturation becomes are reported in table 3.2, while in figure 3.7 are reported the measurements. The DrR is then defined as the ratio between the signal response of each dosimeters at a fixed DDP of 1 cGy/p and is called dosimeter reading ratio (DrR):

$$DrR = \frac{R}{R|_{Dp=1cGy/p}} = \frac{R}{R_{ref}} \quad (3.2)$$

Then, for a saturation not affected by saturation problems DrR should be a straight line with a slope equal to 1; since the reference measurements of dose has been performed with radiochromic films (GAFCHROMIC EBT-XD), whose dose independence has been tested⁶

⁵This is called Raether-Meek condition

⁶The radiochromic films calibration has been obtained by irradiating the films with dose values in range

Commercial detector	Detector type	saturation [Gy/p]
PTW TW34045 Advanced Markus EC	ionization chamber	0.3
PTW TM60017 Dosimetry Diode E	silicon diode	0.15
PTW TW60019 microDiamond	diamond	0.15
DoseVue DoseWireTM Series 100	scintillator fiber	11-26

Table 3.2: Results obtain in [10]

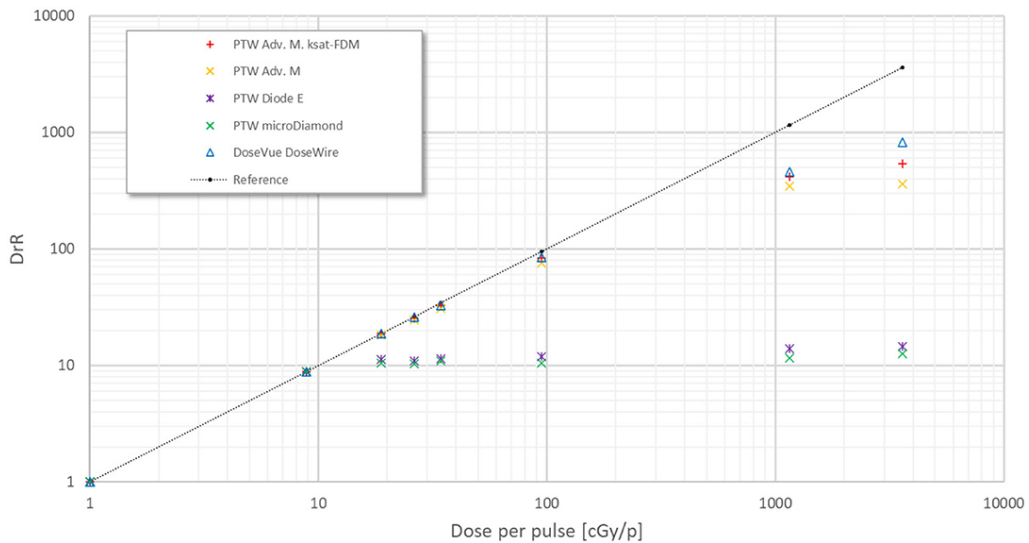


Figure 3.7: Saturation problems underlyed in [10].

708 in range from 0 Gy to 15 Gy, the dotted black line in figure 3.7 represents the reference
709 measurment done with it.

710 Besides the linearity of the response, two other important requirements for beam mon-
711 itoring in radiotherapy are both high temporal and space resolutions. Concerning time
712 resolution I recall that MAPS could handle with rate up to hundreds of MHz, so the pos-
713 sibility application of these detectors probably strictly depends on their particular usage.
714 However MAPS might be well suited given that their spatial resolution and their thinness
715 (they can be thinned down to about 50 μm), which is an obvious requirement for beam
716 monitor.

from 0 Gy to 15 Gy, by positioning the films in a polymethylmethacrylate (PMMA) phantom at R_{100} depth,
corresponding to 10 cm

⁷¹⁷ **Chapter 4**

⁷¹⁸ **TJ-Monopix1**

⁷¹⁹ TJ-Monopix1 is a small electrode DMAPS with fast R/O capability, fabricated by Tow-
⁷²⁰ erJazz foundry in 180 nm CMOS imaging process. It is part, together with prototypes
⁷²¹ from other series such as TJ-MALTA, of the ongoing R&D efforts aimed at developing
⁷²² DMAPS in commercial CMOS processes, that could cope with the requirements at ac-
⁷²³ celerator experiments. Both TJ-Monopix and TJ-MALTA series [11], produced with the
⁷²⁴ same technology by TowerJazz (the timeline of the foundry products is shown in figure
⁷²⁵ 4.1), are small electrode demonstrators and principally differ in the readout design: while
⁷²⁶ Monopix implements a column-drain R/O, an asynchronous R/O without any distribution
⁷²⁷ of BCID has been used by TJ-Malta in order to reduce power consumption.



Figure 4.1: Timeline in TowerJazz productions in 180 nm CMOS imaging process

⁷²⁸ Another Monopix series, but in 150 nm CMOS technology, has been produced by
⁷²⁹ LFoundry [12]. The main differences between the LF-Monopix1 and the TJ-Monopix1
⁷³⁰ (summarized in table 4.2), lay in the sensor rather than in the readout architecture, as
⁷³¹ both chips implements a fast column drain R/O with ToT capability [13][14]. Concerning

	LF-Monopix1	TJ-Monopix1
Resistivity	$>2 \text{ k}\Omega\text{cm}$	$>1 \text{ k}\Omega\text{cm}$
Pixel size	$50 \times 250 \mu\text{m}^2$	$36 \times 40 \mu\text{m}^2$
Depth	$100\text{-}750 \mu\text{m}$	$25 \mu\text{m}$
Capacity	$\sim 400 \text{ fF}$	$\sim 3 \text{ fF}$
Preamplifier	charge	voltage
Threshold trimming	on pixel (4-bit DAC)	global threshold
ToT	8 bits	6 bits
Consumption	$\sim 300 \text{ mW/cm}^2$	$\sim 120 \text{ mW/cm}^2$
Threshold	$1500 e^-$	$\sim 270 e^-$
ENC	$100 e^-$	$\sim 30 e^-$

Table 4.1: Main characteristics of Monopix1 produced by TowerJazz and LFoundry [13][14]

732 the sensors, either are based on a p-type substrate, but with slightly different resistivities;
 733 in addition LFoundry pixels are larger, thicker and have a large fill factor (the very deep n-
 734 well covers $\sim 55\%$ of the pixel area). The primary consequence is that LF-Monopix1 pixels
 735 have a higher capacity resulting in higher consumption and noise. As I discussed in section
 736 2.4.1, the fact that LF-Monopix has a large fill factor electrode is expected to improve its
 737 radiation hardness. Indeed, a comparison of the performance of the two chips showed that
 738 TJ-Monopix suffers a comparatively larger degradation of efficiency after irradiation, due
 739 to the low electric field in the pixel corner; on the other hand, a drawback of the large fill
 740 factor in LF-Monopix is a significant cross-talk.

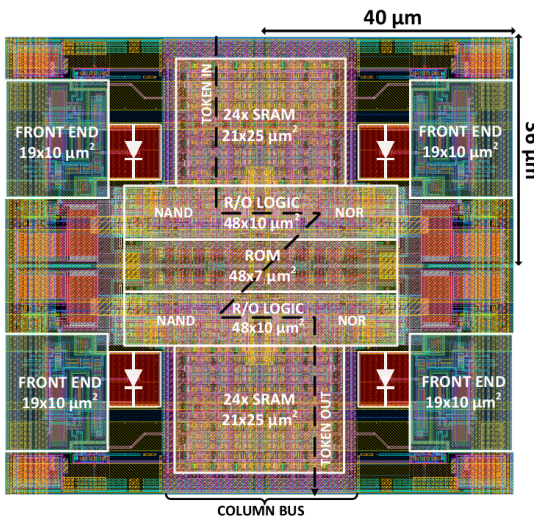
741 The TJ-Monopix1 chip contains, apart from the pixels matrix, all the required support
 742 blocks used for configuration and testing:

- 743 • the whole matrix contains 224×448 pixels, yielding a total active area approximately
 744 equal to 145 mm^2 over a total area of $1 \times 2 \text{ cm}^2$;
- 745 • at the chip periphery are placed some 7-bit Digital to Analog Converter (DAC), used
 746 to generate the analog bias voltage and current levels and to configure the FE;
- 747 • at the EoC is placed a serializer to transfer data immediately, indeed no trigger

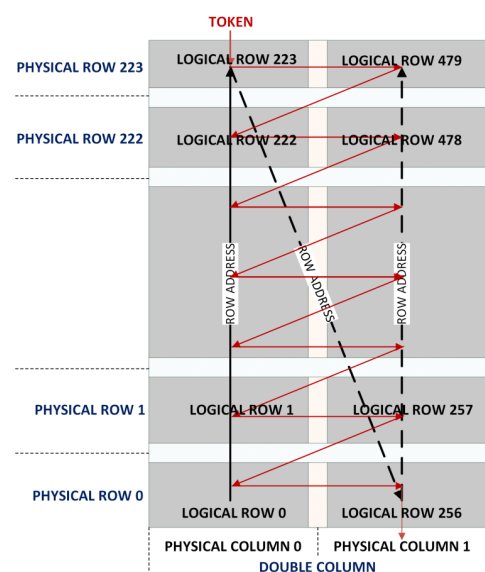
748 memory is implemented in this prototypes;

- 749 • the matrix power pads are distributed at the sides
750 • four pixels which have analog output and which can be monitored with an oscillo-
751 scope, and therefore used for testing

752 Pixels are grouped in 2×2 cores (fig. 4.2a): this layout allows to separate the analog
753 and the digital electronics area in order to reduce the possible interference between the
754 two parts. In addition it simplifies the routing of data as pixels on double column share
755 the same column-bus to EoC. Therefore pixels can be addressed through the physical
756 column/row or through the logical column/row, as shown in fig. 4.2b: in figure is also
757 highlighted the token propagation path, whose I will discuss later.



(a) Layout of a core containing 4 pixels. The analog FE and the digital part are separated in order to reduce cross-talk be



(b)

758 4.1 The sensor

759 As already anticipated, TJ-Monopix1 has a p-type epitaxial layer and a n doped small
760 collection electrode ($2 \mu\text{m}$ in diameter); to avoid the n-wells housing the PMOS transistors
761 competing for the charge collection, a deep p-well substrate, common to all the pixel FE
762 area, is used. TJ-Monopix1 adopts the modification described in section 2.4.2 that allows
763 to achieve a planar depletion region near the electrode applying a relatively small reverse

Parameter	Value
Matrix size	$1 \times 2 \text{cm}^2$
Pixel size	$36 \times 40 \mu\text{m}^2$
Depth	$25 \mu\text{m}$
Electrode size	$2 \mu\text{m}$
BCID	40 MHz
ToT-bit	6
Power consumption	$\sim 120 \text{ mW/cm}^2$

Table 4.2

bias voltage. This modification improves the efficiency of the detector, especially after
 irradiation, however a simulation of the electric field in the sensor, made with the software
 TCAD (Technology Computer Aided Design), shows that a nonuniform field is still pro-
 duced in the lateral regions of the pixel compromising the efficiency at the corner. Two
 variations to the process have been proposed in order to further enhance the transversal
 component of electric field at the pixel borders: on a sample of chip, which includes the one
 in Pisa, a portion of low dose implant has been removed, creating a step discontinuity in the
 deep p-well corner (fig. 4.3); the second solution proposed [**MOUSTAKAS THESYS**,
PAG 58] consists in adding an extra deep p-well near the pixel edge. A side effect of the
 alteration in the low dose implant is that the separation between the deep p-well and the
 p-substrate becomes weak to the point that they cannot be biased separately to prevent
 the punchthrough.

Moreover, to investigate the charge collection properties, pixels within the matrix are
 split between bottom top half and bottom half and feature a variation in the coverage of
 the deep p-well: the electronics area can be fully covered or not. In particular the pixels
 belonging to rows from 0 to 111 are fully covered (FDPW) and pixels belonging to rows
 from 112 to 223 have a reduced p-well (RDPW), resulting in a enhancement of the lateral
 component of the electric field.

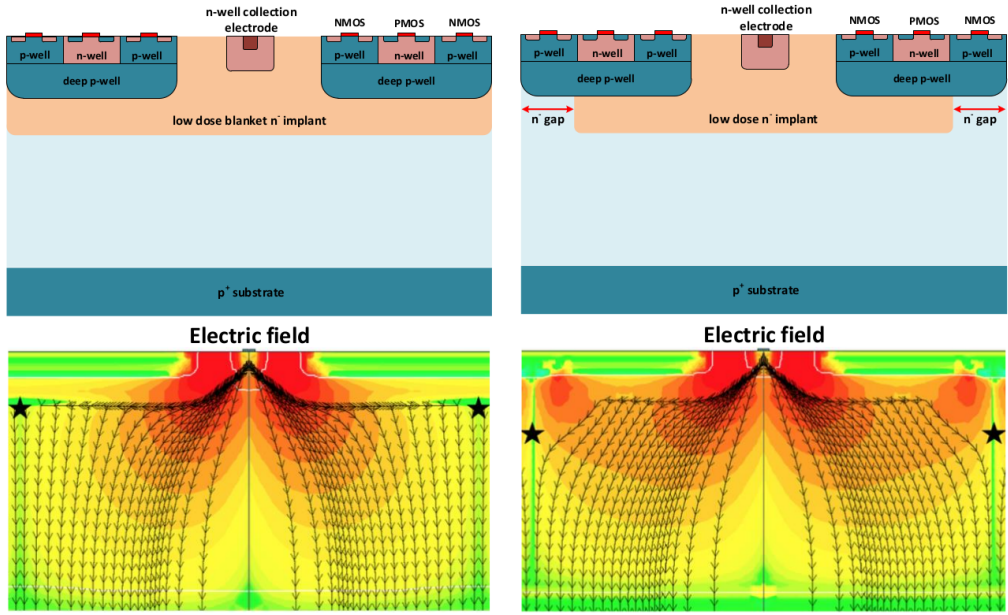


Figure 4.3: (a) The cross-section of a monolithic pixel in the TJ-Monopix with modified process; additionally in (b) a gap in the low dose implant is created to improve the collection of charge due to a bigger lateral component of the electric field. this point in figure is indicated by a star . transversal component of the electric field drops at the pixel corner

782 4.2 Front end

783 The matrix is split in four sections, each one corresponding to a different flavor of the FE.
 784 The four variation have been implemented in order to test the data-bus readout circuits
 785 and the input reset modes.

786 All the flavors implement a source-follower double-column bus readout: the standard
 787 variation is the flavor B, that features a PMOS input reset (refered as "PMOS reset").
 788 Flavor A is identical to flavor B except for the realization of the source follower (it is a
 789 gated one) that aim to reduce the power consumption.**cosa significa?** C instead implements
 790 a novel leakage compensation circuit. Moreover the collection electrode in flavors A, B, C
 791 is DC-coupled to the front-end input, while in D is AC-coupled, providing to applu a high
 792 bias voltage; for this reason flavor D il called "HV flavor".

793 **Principio generale:** R resistenza di reset deve essere abbastanza grande in modo da
 794 far si che il ritorno allo zero è abbastanza lento (non devi "interferire" con la tot slope e

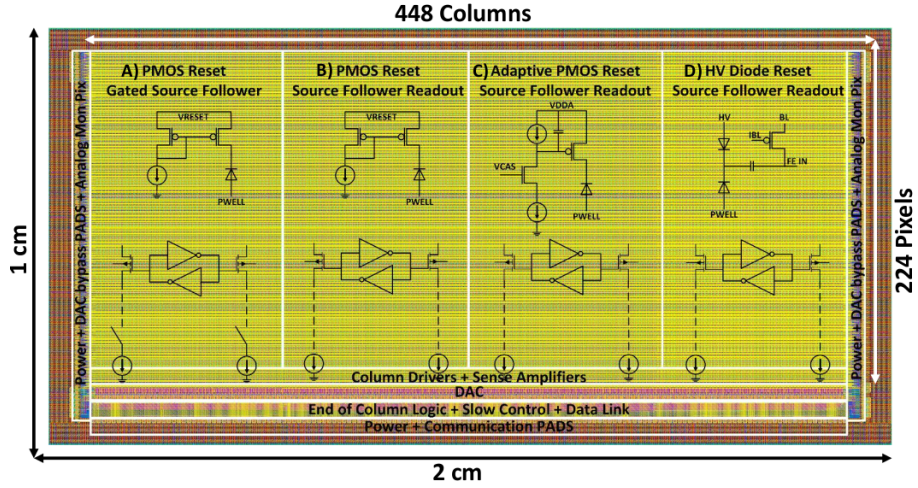


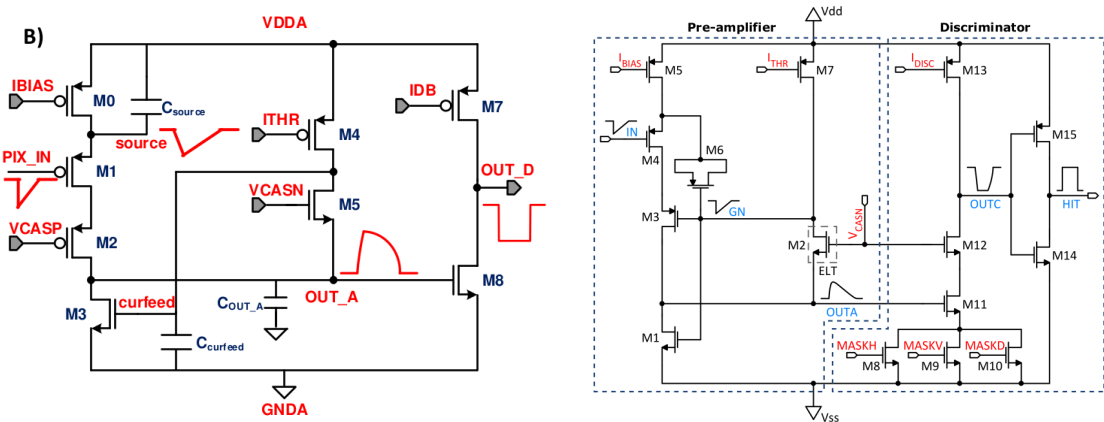
Figure 4.4

795 non deve essere più corto del tempo del preamplificatore, sennò hai perdita di segnale).

796 Baseline reset: all'input solitamente hai un PMOSS o un diodo; R reset

797 4.2.1 ALPIDE-like

798 ALPIDE chips, developed by the ALICE collaboration, implemented a standard FE to the
 799 point that many CMOS MAPS detectors used a similar FE and are called "ALIPDE-like".
 800 Considering that both TJ-Monopix1 and ARCADIA-MD1 have an ALPIDE-like FE, I am
 going to explain the broad principles of the early FE stage. The general idea is of the



(a) ALPIDE-like

(b)

801

802 amplification to transfer the charge from a bigger capacity[15], C_{source} , to a smaller one,
 803 C_{out} : the input transistor M1 with current source IBIAS acts as a source follower and this

804 forces the source of M1 to be equal to the gate input $\Delta V_{PIX_IN} = Q_{IN}/C_{IN}$.

$$Q_{source} = C_{source} \Delta V_{PIX_IN} \quad (4.1)$$

805 The current in M2 and the charge accumulates on C_{out} is fixed by the one on C_{source} :

$$\Delta V_{OUT_A} = \frac{Q_{source}}{C_{OUT_A}} = \frac{C_{source} \Delta V_{PIX_IN}}{C_{OUT_A}} = \frac{C_{source}}{C_{OUT_A}} \frac{Q_{IN}}{C_{IN}} \quad (4.2)$$

806 A second branch (M4, M5) is used to generate a low frequency feedback, where VCASN
807 and ITHR set the baseline value of the signal on C_{OUT_A} and the velocity to goes down
808 to the baseline.

809 **IL RUOLO DI CURVFEED NON L'HO CAPITO.**

810 Finally IDB defines the charge threshold with which the signal OUT_A must be compared:
811 depending on if the signal is higher than the threshold or not, the OUT_D is high or low
812 respectively.

813 The actual circuit implemented in TJ-Monopix1 is shown in figure 4.5b: the principal
814 difference lays in the addition of disableing pixels' readout. This possibility is uttermost
815 important in order to reduce the hit rate and to avoid saturating the bandwidth due to the
816 noisy pixels, which typically are those with manufacturing defects. In the circuit transis-
817 tors M8, M9 and M10 have the function of disabling registers with coordinates MASKH,
818 MASKV and MASKD (respectively vertical, orizontal and diagonal) from readout: if all
819 three transistors-signals are low, the pixel's discriminator is disabled. Compared with a
820 configurable masking register which would allow disableing pixels individually, to use a
821 triple redundancy reduces the sensistivity to SEU but also gives amount of intentionally
822 masked ("ghost") pixels. This approach is suitable only for extremely small number N of
823 pixel has to be masked: if two coordinate projection scheme had been implemented, the
824 number of ghost pixels would have scale with N^2 , if instead three coordinates are used,
825 the N's exponential is lower than 2 (fig. 4.6)

826 **4.3 Readout logic**

827 TJ-Monopix1 has a triggerless, fast and with ToT capability R/O which is based on a
828 column-drain architecture. On the pixel are located two Random Access Memory (RAM)
829 cells to store the 6-bit LE and 6-bit TE of the pulse, and a Read-Only Memory (ROM)

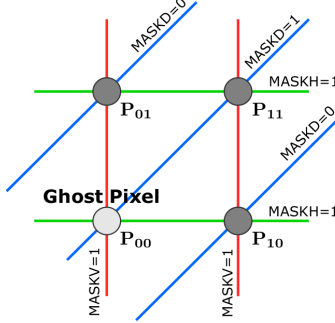


Figure 4.6

Parameter	Meaning	
IBIAS	mainly controls the rise time	yes? check
IDB	sets the discriminator threshold	yes
ITHR	sets the velocity of the return to the baseline	yes
ICASN	sets the baseline of the signal	yes
VRESET	sets the gain of the preamplifier	yes
IRESET	sets the gain of the preamplifier	no

Table 4.3: FE parameters which must be setted through the DAQ. "Function" means that higher parameter implies higher value

830 containing the 9-bit pixel address. Excluded these memories, TJ-Monopix1 hasn't any
 831 other buffer: if a hit arrives while the pixel is already storing a previous one, the new
 832 data get lost. After being read, the data packet is sent to the EoC periphery of the
 833 matrix, where a serializer transfers it off-chip to an FPGA (4.7). There a FIFO is used
 834 to temporarily stored the data, which is transmitted to a computer through an ethernet
 835 cable in a later time.

836 The access to the pixels' memory and the transmission of the data to the EoC, following
 837 a priority chain, is managed by control signals and is based on a Finite State Machine
 838 (FSM) composed by four state: no-operation (NOP), freeze (FRZ), read (RD) and data
 839 transfer (DTA). The readout sequence (??) starts with the TE of a pulse: the pixel
 840 immediately tries to grab the column-bus turning up a hit flag signal called *token*. The
 841 token is used to control the priority chain and propagates across the column indicating

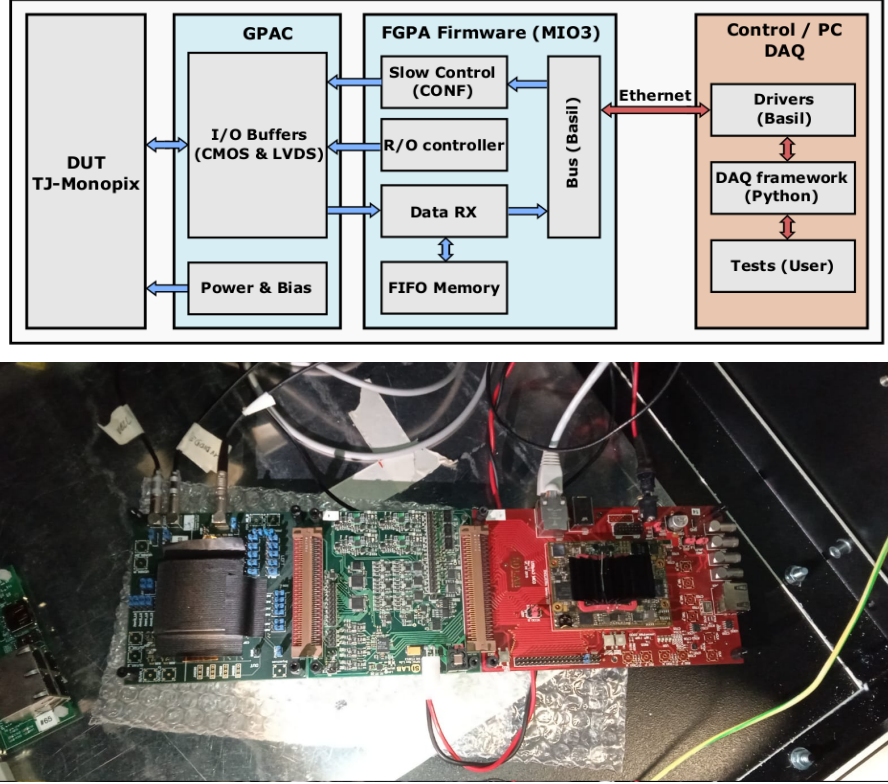


Figure 4.7: Main caption

842 what pixel that must be read. To start the readout and avoid that the arrival of new hits
 843 disrupt the priority logic, a *freeze* signal is activated, and then a *read* signal controls the
 844 readout and the access to memory. During the freeze, the state of the token for all pixels
 845 on the matrix remains settled: this does not forbid new hits on other pixels from being
 846 recorded, but forbids pixels hit from turning on the token until the freeze is ended. The
 847 freeze stays on until the token covers the whole priority chain and gets the EoC: during
 848 that time new token cannot be turned on, and all hits arrived during a freeze will turn
 849 on their token at the end of the previous freeze. Since the start of the token is used to
 850 assign a timestamp to the hit, the token time has a direct impact on the time resolution
 851 measurement; this could be a problem coping with high hits rate.

852 The analog FE circuit and the pixel control logic are connected by an edge detector
 853 which is used to determine the LE and the TE of the hit pulse(fig. 4.9): when the TE
 854 is stored in the first latch the edge detector is disabled and, if the **FREEZE** signal is not
 855 set yet, the readout starts. At this point the HIT flag is set in a second latch and a token
 856 signal is produced and depending on the value of **Token** in the pixel can be read or must

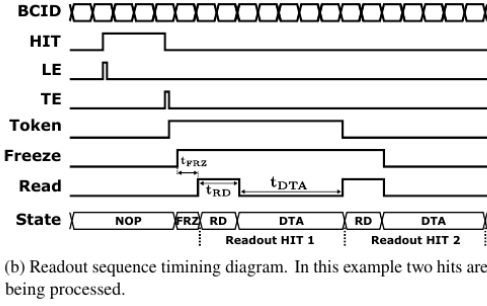


Figure 4.8: Readout timing diagram: in this example two hits are being processed

857 wait until the **Token in** is off. In figure an OR is used to manage the token propagation, but
 858 since a native OR logic port cannot be implemented with CMOS logic, a sum of a NOR
 859 and of an inverter is actually used; this construct significantly increases the propagation
 860 delay (the timing dispersion along a column of 0.1-0.2 ns) of the token and to speed up
 861 the circuit optimized solution are often implemented. When the pixel become the next to
 862 be read in the queue, and at the rising edge of the **READ** signal, the state of the pixel is
 863 stored in a D-latch and the pixel is allowed to use the data bus; the TE and the HIT flag
 864 latches are reset and a **READINT** signal that enable access of the RAM and ROM cells
 865 is produced.

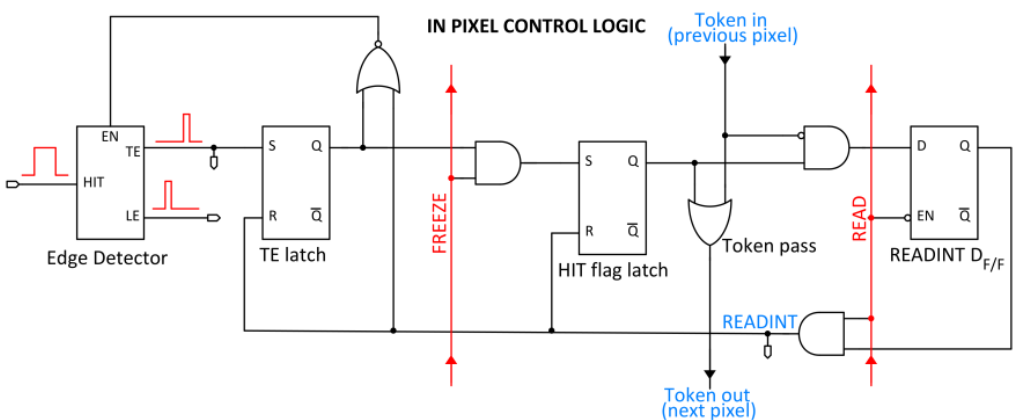


Figure 4.9

866

867 The final data must provide all the hits' information: the pixel address, the ToT and
 868 the timestamp. All those parts are assigned and appended at different time during the
 869 R/O chain:

- **Pixel address:** while the double column address (6-bit) is appended by the EoC

871 circuit, the row address (8-bits for each flavor) and the physical column in the doublet
872 (1-bit) are assigned by the in-pixel logic

- 873 • **ToT:** is obtained offline from the difference of 6-bits TE and 6-bits LE, stored by
874 the edge detector in-pixel; since a 40 MHz BCID is distributed across the matrix,
875 the ToT value is range 0-64 clock cycle which corresponds to 0-1.6 μ s
- 876 • **Timestamp:** The timestamp of the hit correspond to the time when the pixel set
877 up the token; it is assigned by the FPGA, that uses the LE, TE and a 640 MHz
878 clock to derive it. For all those hits which arrived while the matrix is frozen, the
879 timestamp is no more correlated with the time of arrival of the particle

880 When the bits are joined up together the complete hit data packet is 27-bit.

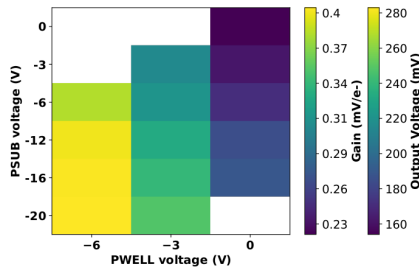


Figure 4.10: 2D map of the output voltage amplitude and gain with respect to the p-well
and p-substrate in the case of the PMOS reset front-end

881 Measurement of the magnitude of the collected charge has also been generally available
882 for pixel detectors, and has been used to improve the 3D space point precision through
883 interpolation as well as for particle identification through specific ionization measurement.

884 **Chapter 5**

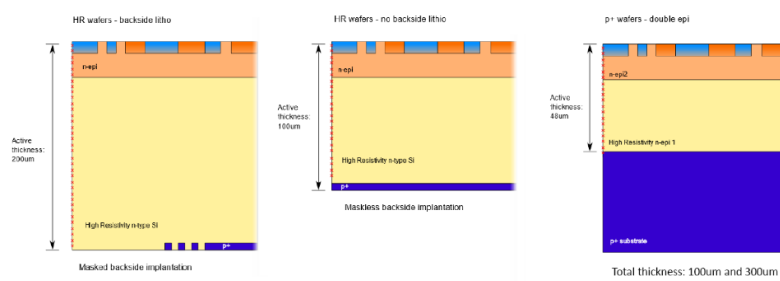
885 **Arcadia-MD1**

886 [16] [17]

887 Breve introduzione analoga a Monopix1 in cui descrivo brevemente la "timeline" da
888 SEED Matisse a Md1 e Md2

889 **5.1 The sensor**

890 ARCADIA-MD1 is an LFoundry chip which implements the technology 110 nm CMOS
891 node with six metal layer ??. The standard p-type substrate was replaced with an n-type
892 floating zone material, that is a technique to produce purified silicon crystal. (pag 299
893 K.W.).



894 Figure 5.1

895 Wafer thinning and backside lithography were necessary to introduce a junction at the
896 bottom surface, used to bias the substrate to full depletion while maintaining a low voltage
897 at the front side.

898 C'è un deep pwell per - priority chainseparare l'elettronica dal sensore; per controllare il
899 punchthought è stato aggiunto un n doped epitaxial layer having a resistivity lower than
900 the substrate.

901 RILEGGI SUL KOLANOSKY COS'È IL PUNCHTHROUGHT, FLOAT ZONE MA-
902 TERIAL, COME VENGONO FATTI I MAPS COME FAI LE GIUNZIONI

903 It is part of the cathegory of DMAPS Small electrode to enhance the signal to noise
904 ratio.

905 It is operated in full depletion with fast charge collection by drift.

906 Prima SEED si occupa di studiare le prestazioni: oncept study with small-scale test
907 structure (SEED), dopo arcadia: technology demonstration with large area sensors Small
908 scale demo SEED(sensor with embedded electronic developement) Quanto spazio dato
909 all'elettronica sopra il pwell e quanto al diodo. ..

910 5.2 Readout logic and data structure

911 5.2.1 Matrix division and data-packets

912 The matrix is divided into an internal physical and logical hierarchy: The 512 columns are
913 divided in 16 section: each section has different voltage-bias + serializzatori. Each section
914 is devided in cores () in modo che in ogni doppia colonna ci siano 1Pacchetto dei dati 6
915 cores. ricordati dei serializzaatori: sono 16 ma possono essere ridotti ad uno in modalità
spazio

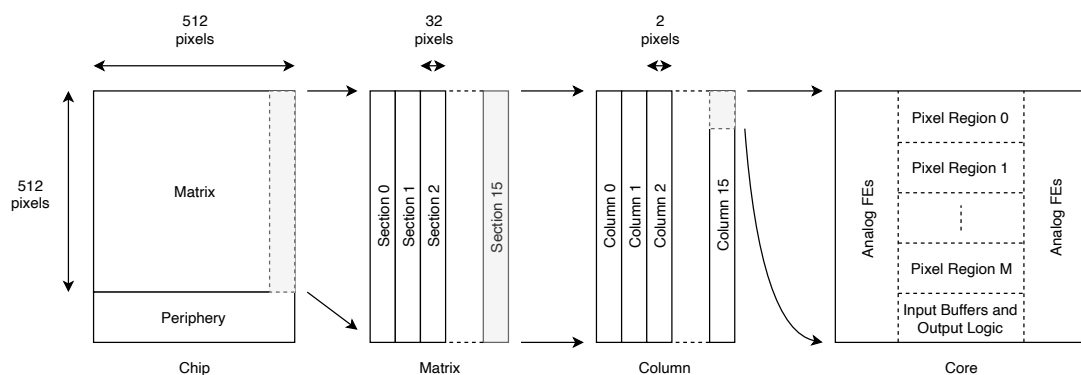


Figure 5.2

916

917 Questa divisione si rispecchia in come sono fatti i dati: scrivi da quanti bit un dato è

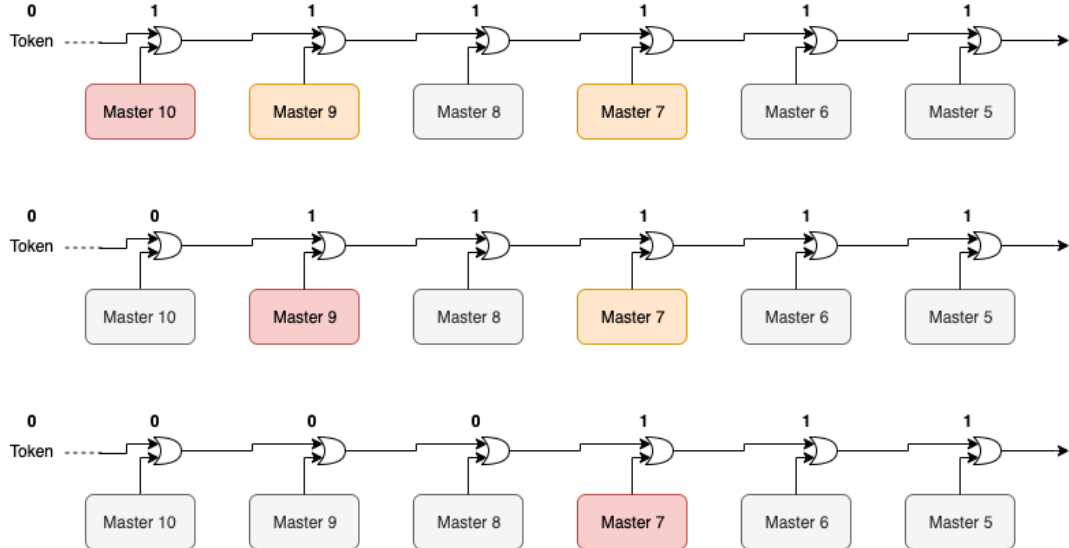


Figure 5.3

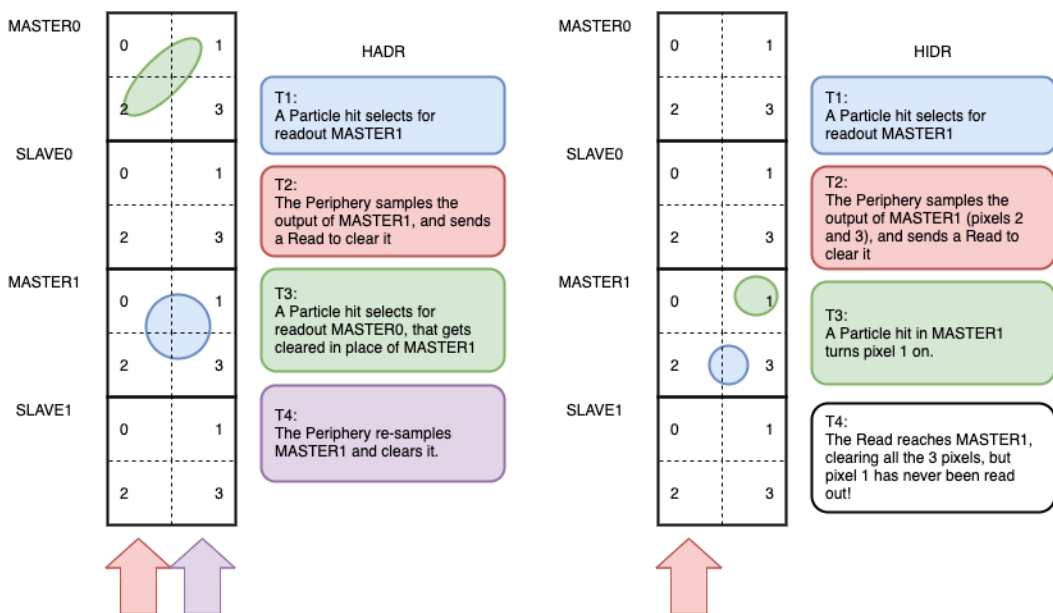


Figure 5.4

918 fatto e le varie coordinate che ci si trovano dentro; devi dire che c'è un pixel hot e spieghi
 919 dopo a cosa serve, e devi accennare al timestamp

920 "A core is simply the smallest stepped and repeated instance of digital circuitry. A
 921 relatively large core allows one to take full advantage of digital synthesis tools to imple-
 922 ment complex functionality in the pixel matrix, sharing resources among many pixels as
 923 needed.". pagina 28 della review.

924

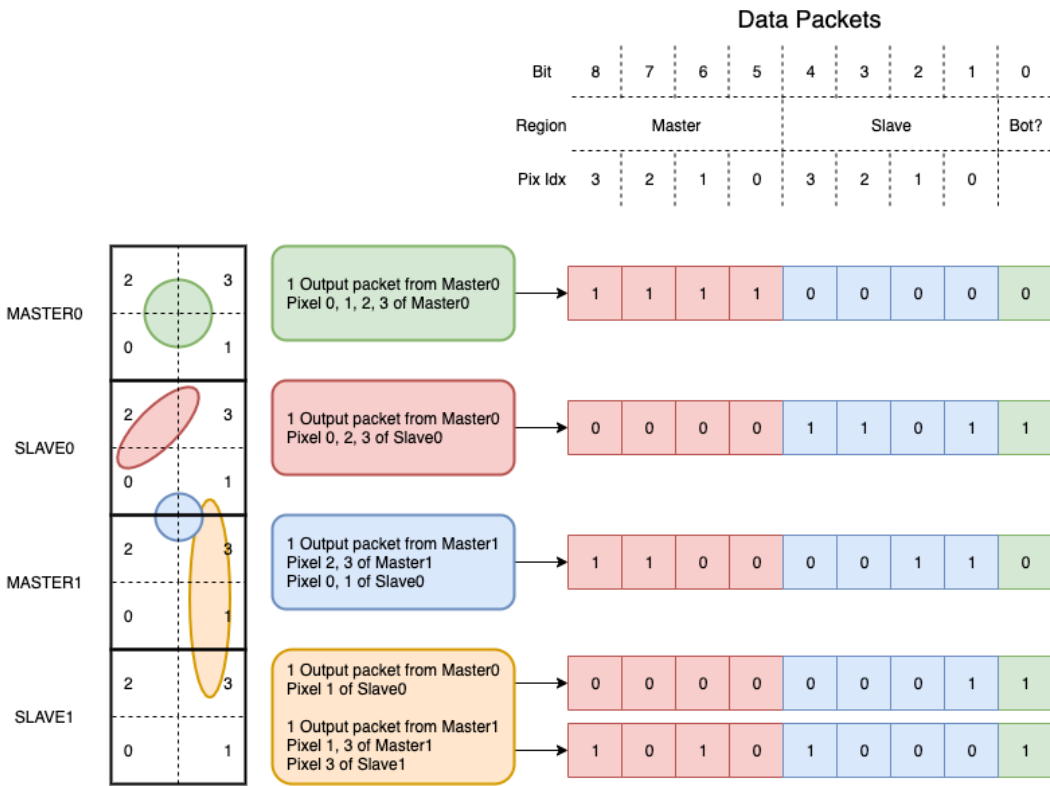


Figure 5.5

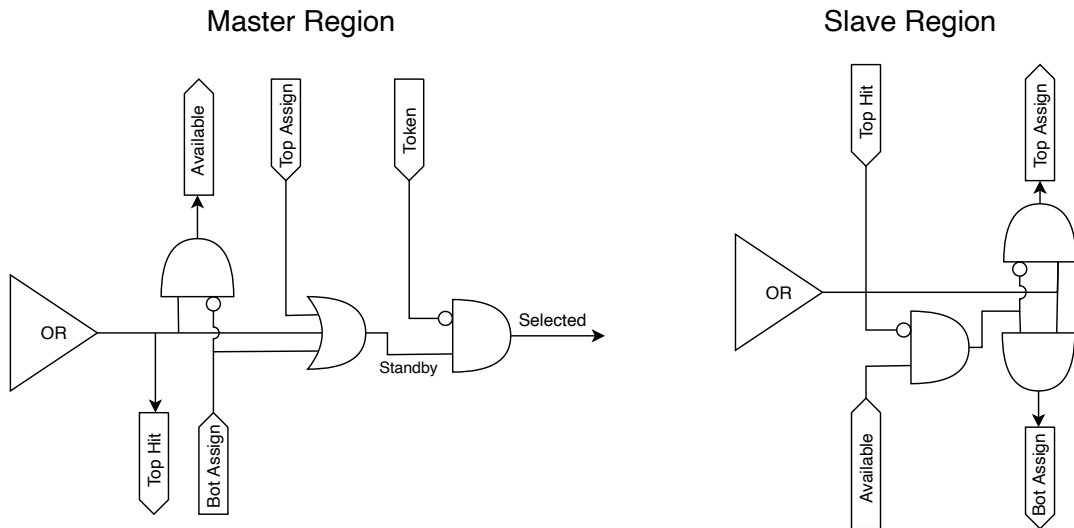


Figure 5.6

925 TABELLA: con la gerarchia del chip Matrix (512x512 pixels) Section (512x32 pixels)

926 Column (512x2) Core (32x2) Region (4x2)

927 Nel chip trovi diverse padframe: cosa c'è nelle padframe e End of section.

928 "DC-balance avoids low frequencies by guaranteeing at least one transition every n
929 bits; for example 8b10b encoding n =5"

930 **Chapter 6**

931 **Characterization**

932 rifai il conto della lunghezza di attenuazione. Ho trovato (presentazione Luciano Mus) 29
933 um per ka e 37 um per kb.

934 **6.1 TJ-Monopix1 characterization**

935 **6.1.1 Threshold and noise: figure of merit for pixel detectors**

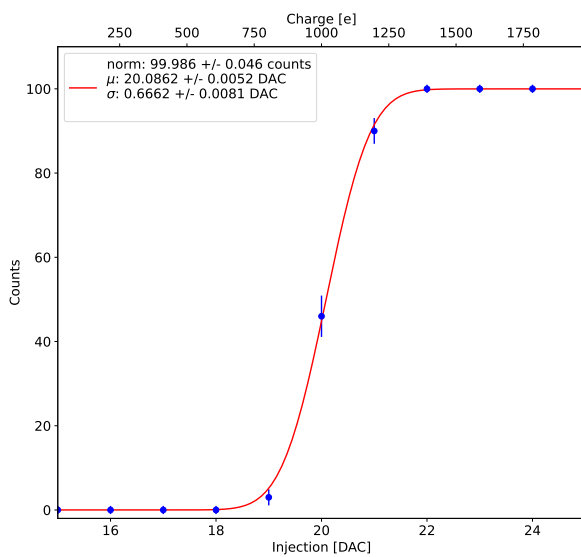


Figure 6.1: S-curve for pixel (10, 10) of the PMOS flavor (flavor 1) with IDB fixed at 40 DAC. The conversion of charge injected from DAC to electrons has been done assuming a conversion factor of $20 \text{ e}^-/\text{DAC}$.

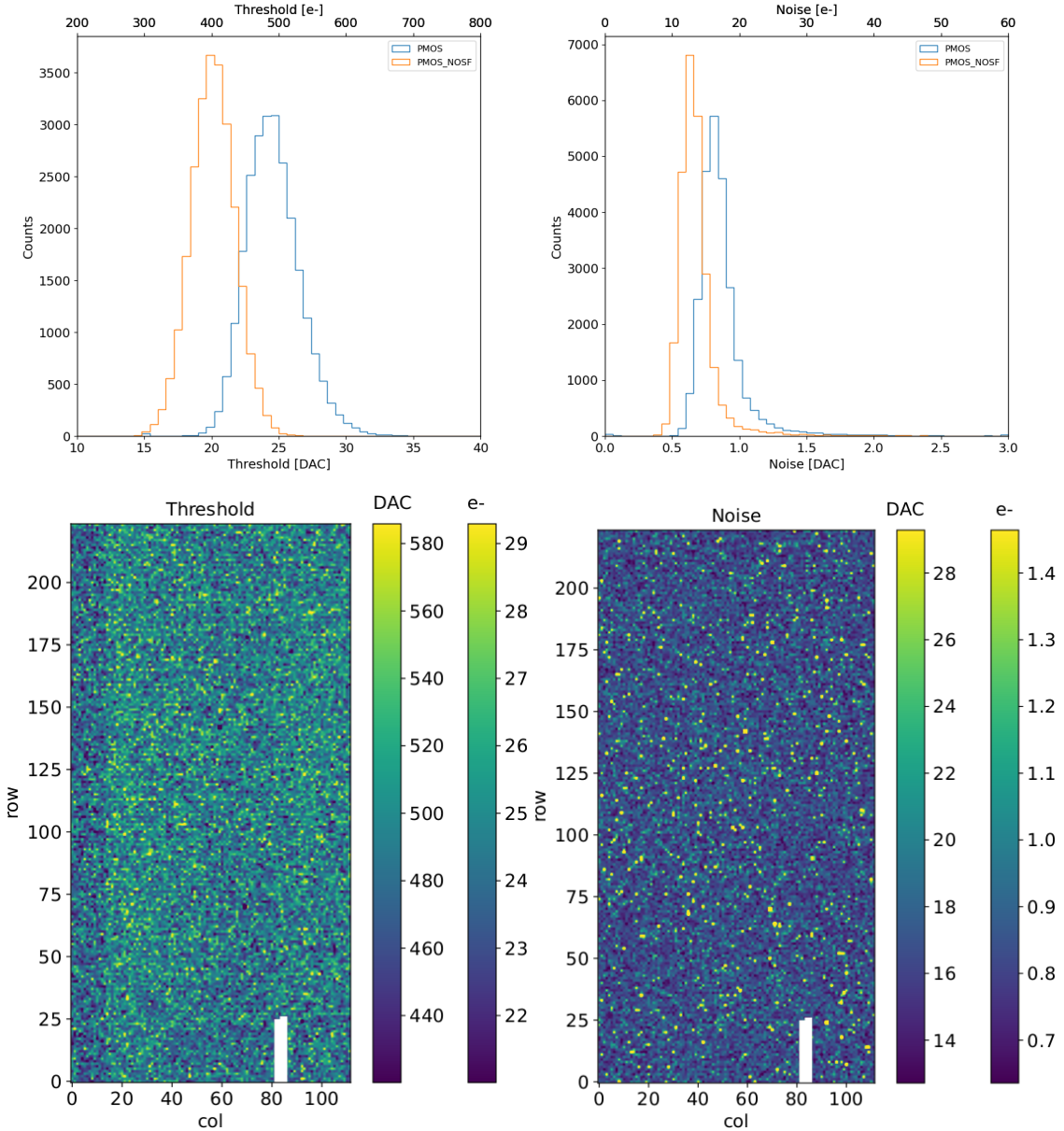


Figure 6.2: Histograms of the threshold (a) and the noise (b) found fitting the s-curve of all flavor with IDB fixed at 40 DAC. Maps of the threshold (a) and the noise (b) found fitting the s-curve with IDB fixed at 40 DAC. The white pixels have the injection circuit broken.

936 A characterization of threshold and noise is typically necessary since these values have
 937 an impact on the operating conditions and on the performance of the chips. infact, the
 938 signal to threshold ratio may be considered as the figure of merit for pixel detectors rather
 939 than the signal to noise ratio. The mean minimum stable threshold evolved through
 940 different generation of chips: in the 1st generation it was around 2500 e⁻ while in the

941 3rd (corresponding to nowadays chips) is less than 500 e^- . This allows in thinner sensors
 942 with smaller signals: from $16\,000 \text{ e}^-$ produced in $200 \mu\text{m}$, the signal expected moved down
 943 to 2000 e^- produced in $25 \mu\text{m}$. According with this ??, the threshold of TJ-Monopix1 is
 944 around 500 e^- . The following prototypes have lower threshold and noise, for example TJ-
 945 Monopix2 has check, according to the above. The threshold has to be located between the
 946 noise peak around the baseline and the signal distribution, in particular it has to be low
 947 enough to mantain a high signal efficiency, but also high enough to cut the noise: for a low
 948 threshold many pixels can fire at the same time and a positive feedback can set off a chain
 949 reaction eventually, causing all the other pixels to fire. Thus, the noise sets a lower bound
 950 to the threshold: if an occupancy $\leq 10^{-4}$ is required, for example, this correspond to the
 951 Gaussian 1-sided tail fraction for 3.7σ . In this case, if the noise is 100 e^- , for example, the
 952 threshold must be higher than $3.7 \times 100 \text{ e}^-$. Typically this argument sets only a minimal
 953 bound to the threshold since the variation with time and from pixel to pixel have to be
 954 taken into account: the temperature, the annealing (for example, the radiation damages in
 955 the oxide layer causes shift of MOSFET threshold voltage) and the process parameters
 956 variation across the wafer (as for example process mismatch between transistors).

957 On the other hand the noise is valued at the preamplifier input node given that the
 958 first stage of amplification is the most crucial since the signal amplitude is high compared
 959 to additional noise introduced by the following stages. The noise is then parameterized as
 960 Equivalent Noise Charge (ENC), which is defined as the ratio between the noise N at the
 961 output expressed in Volt and the out voltage signal S produced by 1 e^- entering in the
 962 preamplifier:

$$ENC = \frac{N_{out}[\text{V}]}{S_{out}[\text{V}/\text{e}^-]} = \frac{V_{noise}^{RMS}}{G} \quad (6.1)$$

963 with G expressed in V/e^- ; as the gain increases, the noise reduces .

964 ENC is mainly influenced by the total input capacitance and by the system band-
 965 width: if the bandwidth is constant, noise can be reduced by increasing the input transis-
 966 tor transconductance (and consequently power consumption). Considering the threshold
 967 dispersion a requirement for the ENC is:

$$ENC < \sqrt{(T/3.7)^2 - T_{RMS}^2(x) - T_{RMS}^2(t)} \quad (6.2)$$

968 where the T is the threshold set, T_{RMS} is the threshold variation during time (t) and

969 across the matrix (x); a typical reasonable value often chosen is 5 ENC.

970 Because of the changing of the 'real' threshold, the possibility of changing and adapting
971 the setting parameters of the FE, both in time and in space is desiderable: these parameters
972 are usually set by Digital to Analog Converter (DAC) with a number of bit in a typical
973 range of 3-7. Unfortunately DAC elements require a lot of space that may be not enough
974 on the pixel area; therefore, the FE parameters are typically global, which means that they
975 are assigned for the whole chip, or they can be assigned for regions the matrix is divided
976 into. The former case corresponds to TJ-Monopix1's design in which 7 bits are used for
977 a total 127-DAC possible values, while the latter corresponds to the ARCADIA-MD1's
978 one, **where quanti bit??**. An other possibility, for example implemented in TJ-Monopix2,
979 is allocate the space on each pixel for a subset of bits, then combinig the global threshold
980 with a fine tuning. If so, the threshold dispersion after tuning is expected to be inversely
981 proportional to the tuning DAC number of bits and thus be improved a lot:

$$\sigma_{THR,tuned} = \frac{\sigma_{THR}}{2^{nbit}} \quad (6.3)$$

982 where σ_{thr} is the RMS of the threshold spread before tuning.

983 To measure the threshold and noise of pixels a possible way is to make a scan with
984 different known injected charge: the threshold corresponds to the value where the efficiency
985 of the signal exceeds the 50%, and the ENC is determined from the width of this edge.
986 Following this path, I have used the injection circuit available on the chip to inject 100
987 pulses for each input charge for a fixed threshold. The injection comes on a capacity at the
988 input of the FE circuit, whose mean value is 230 aF and from which the conversion factor
989 from DAC units to electrons can be obtained: for the PMOS flavor, for example, since
990 the DAC are biased at 1.8 V, the Least significant Bit (LSB) corresponds to a voltage of
991 14.7 mV from which the charge for LSB $1.43 \text{ e-}/\text{mV}$ and the conversion factor therefore
992 is $20.3 \text{ e-}/\text{DAC}$. While this value is equivalent for all the PMOS flavor, the HV flavor
993 is expected to have a different conversion factor, $\sim 33 \text{ e-}/\text{DAC}$, beacuse of the different
994 input capacity.

995 Besides the charge, also the duration and the period of the injection pulse can be set;
996 it is important to make the duration short enough to have the falling edge during thed
997 dead time of the pixel (in particular during the FREEZE signal) in order to avoid the

	DAC units	electrons
Threshold	24.529 ± 0.049 u: 24.433 ± 0.049 d: 24.623 ± 0.051	
Threshold dispersion	1.848 ± 0.033 u: 1.867 ± 0.034 d: 1.825 ± 0.035	
Noise	0.8222 ± 0.0043 u: 0.8225 ± 0.0045 d: 0.8221 ± 0.0043	
Noise dispersion	0.0975 ± 0.0030 u: 0.0968 ± 0.0031 d: 0.0970 ± 0.0030	

Table 6.1: Flavor PMOS, IDB fixed at 40 DAC

undershoot, coming at high input charge, triggering the readout and reading spurious hits. Since the injection circuit is coupled in AC to the FE, if the falling edge of the pulse is sharp enough to produce an undershoot, this can be seen as a signal.

Assuming a gaussian noise, the efficiency of detecting the signal can be described through a modification of the error function:

$$f(x, \mu, \sigma) = \frac{1}{2} \left(1 + \operatorname{erf} \left(\frac{x - \mu}{\sigma\sqrt{2}} \right) \right) \quad (6.4)$$

with: where the threshold and the ENC corresponds to the μ and σ . Therefore I perform a fit of the counts detected using the function in equation 6.4. In figure 6.1 there is an example with IDB (look at table 6.1 for the meaning of the parameter) equal to 40 DAC of fit for a pixel belonging to the flavor 1, while in table 6.1 and figure ?? and ?? there are the histograms and the maps of the parameters of the scurve-fit.

To verify the trend of the threshold as a function of the front end parameter IDB, I have performed a scan with different IDBs: I have injected the whole matrix and found the means and the standard deviation of the distributions. The results are shown in figure

6.3.

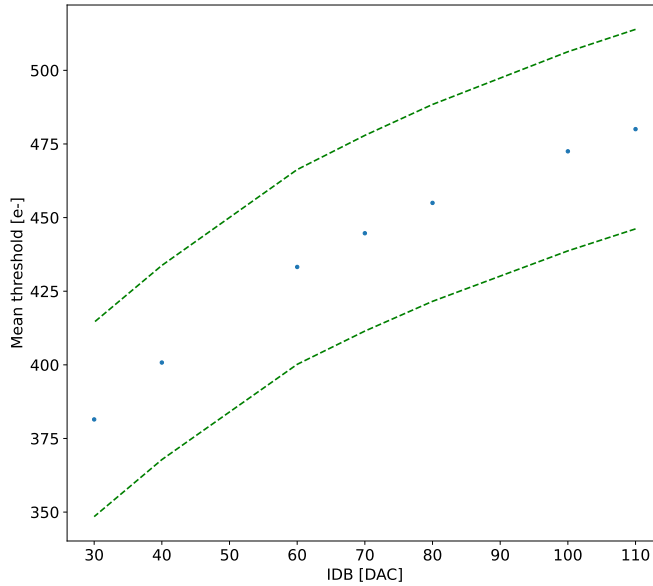


Figure 6.3

1011

1012 6.1.2 Linearity of the ToT

1013 I have already said in chapter 4 that TJ-Monopix1 returns an output signal proportional to
 1014 the charge released by a particle in the epitaxial layer, which is the Time over Threshold;
 1015 the ToT is saved as a 6-bit variable and then has a dynamic range equal to 0-64, which
 1016 corresponds to 0 μ s to 1.6 μ s assuming a clock frequency of 40 MHz. When a pulse is longer
 1017 than 1.6 μ s the counter rolls back to zero and there is no way to distinguish that charge
 1018 from a lower one with the same ToT: that is the rollover of the ToT (??(a)).

1019 In order to associate the ToT (in range 0-64) to the charge, a calibration of the signal
 1020 is necessary. Assuming the linearity between ToT and the charge, Q can be found:

$$Q [DAC] = \frac{(ToT [au] - q [au])}{m [au/DAC]} \quad (6.5)$$

1021 where m and q are the fitted parameters of the calibration. It is important to keep in
 1022 mind that the main application target of TJ-Monopix1 is in the inner tracker detector of
 1023 HEP experiments, then the main feature is the efficiency, then a rough calibration of the
 1024 signal to charge is fine; **this information can be used to improve??.**

	PMOS 0	PMOS 1	PMOS 2	HV
Slope [au/DAC]	0.75566 ± 0.00149	0.57145 ± 0.00025		
Slope dispersion [au/DAC]	0.03841 ± 0.00037	0.01685 ± 0.00016		
Intercept [au]	-11.6070 ± 0.0089	-10.824 ± 0.019		
Intercept dispersion [au]	1.5176 ± 0.0063	1.225 ± 0.013		

Table 6.2: Mean calibration parameters for **all** flavor and their dispersion on the matrix.

1025 The study of the output signal is made possibile via the injection: since the pulses
 1026 are triangular, the ToT is expected to be almost linear depending on the injection charge
 1027 value. To verify this statement and study the deviations from linearity I've fit the ToT
 1028 versus the charge injected for all pixel within the matrix. In figure ??(b) there is an
 1029 example of fit for a pixel belonging to the flavor 1, while in figure 6.5 and ?? there are the
 1030 histograms and the maps of the parameters of the line-fit for all flavors with IDB fixed at
 1031 40 DAC.

1032 Before performing the fit I have calculated the mean value of the ToT of the pulses
 1033 recorded for each pulse amplitude and I used the mean ToT as value for the fit. The aim
 1034 of the calibration obviously is finding a relation only in the range 0-64 without taking into
 1035 account the rolling over hits: therefore, to prevent the rollover data from reducing the
 1036 mean ToT introducing a bias in the mean value, I cut and I did not consider them. If a
 1037 signal bigger than the $1.6 \mu s$ is expected in the usage of the detector, the threshold must be
 1038 raised or the gain reduced, making the expected output signal in range 0-64. In figure ??
 1039 (b) are shown both the fits with a line (red) and with a second order polynomial (green):
 1040 at the bounds of the ToT range values deviate from the line model. Since the deviation is
 1041 low than **controlla quant'era, questo ha un impatto sul valore della calibrazione di tipo ..**
 1042 **che è trascurabile al primo ordine. e comunque hai problemi ai bounds mentre al centro**
 1043 **hai comunque una buona linearità.. Chiarire la differenze negli istogrammi e come mai ci**
 1044 **sono delle bande nelle mappe.**

1045 perchè noise e th sono diverse per diversi flavor? Controlla cos' hanno di diverso.

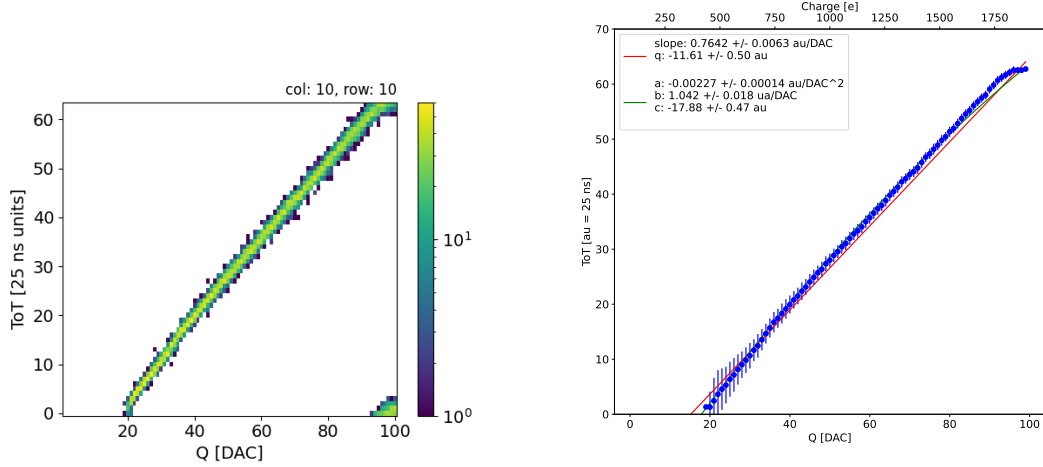


Figure 6.4: The figures refer to pixel (10,10) of the PMOS-reset flavor (1) with IDB fixed at 40 DAC. (a) Histogram of the injection pulses: the ToT is in range 0-64 since it is represented by 6 bit, so when achieving the 64 it rolls over back to the zero. (b) Mean ToT vs the the charge: the mean has been calculated cutted the rolling hits.

6.1.3 Calibration of the ToT

Considering that the charge injected in the FE goes to fill capacitor which is different from pixel to pixel, the true charge injected does not correspond to what expected assuming C equal to 230 aF, the nominal value. Accordingly to that, a verification of the value provided and an absolute calibration of this capacity and of the conversion factor F is needed to have a correspondence of the signal in electrons; assuming C 230 aF, F is expected to be 20 e-/DAC, and is defined as:

$$F [e- / DAC] = \frac{1616 e-}{Q [DAC]} \quad (6.6)$$

For this pourpose a Fe55 radioactive source has been employed; the Fe55 is en extremely important radionuclide in the calibration of X-ray spectrometers, proportional counter and scintillator detector since it emits two two X-photons during the electron capture decay: the first one (K_{α}) at 5.9 keV and the second one (K_{β}) at 6.5 keV. The K_{α} photon, which does photoelectric effect in the silicium, has an absorption length $\lambda=7 \mu m$ to $8 \mu m$, and the probability of being assorbed in the $25 \mu m$ thick epitaxyal layer is ~ 0.95 . The electron emitted has an energy equal to the photon one, so recalling that the mean energy needed to produce a couple electron-vacuum is 3.65 eV, the signal produced by the Fe55

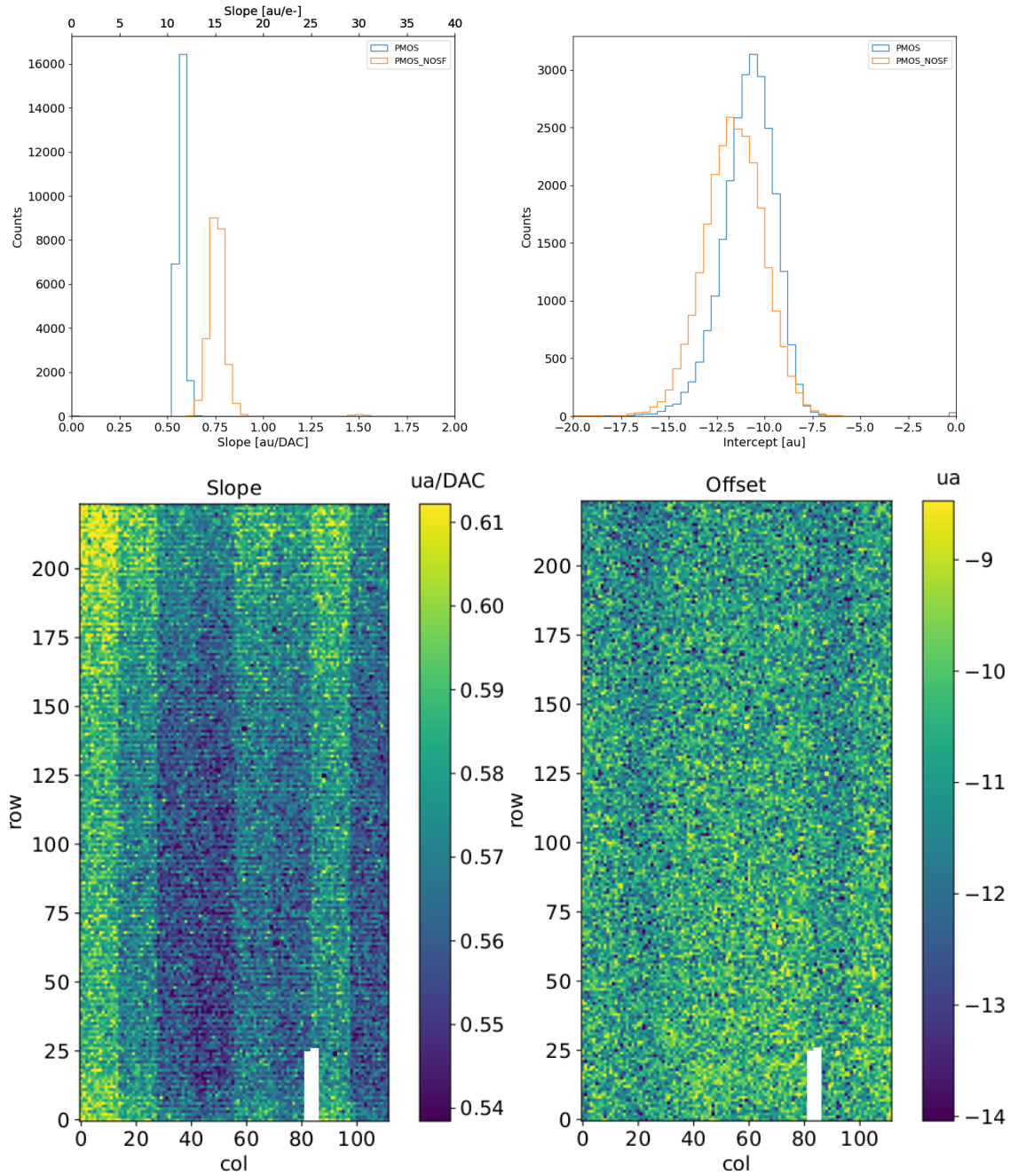


Figure 6.5: Histograms of the calibration parameters, slope (a) and offset (b), found fitting the ToT with a line, for all flavor and with IDB fixed at 40 DAC. Maps of the calibration parameters, slope (a) and offset (b), found fitting the ToT with a line, with IDB fixed at 40 DAC

source is expected to be 1616 e⁻. In figures ?? and ?? are shown two histograms of the ToT spectrum of the Fe55 source for two different pixels. The peak corresponds to the events with completely absorption of the charge produced in the depleted region, while

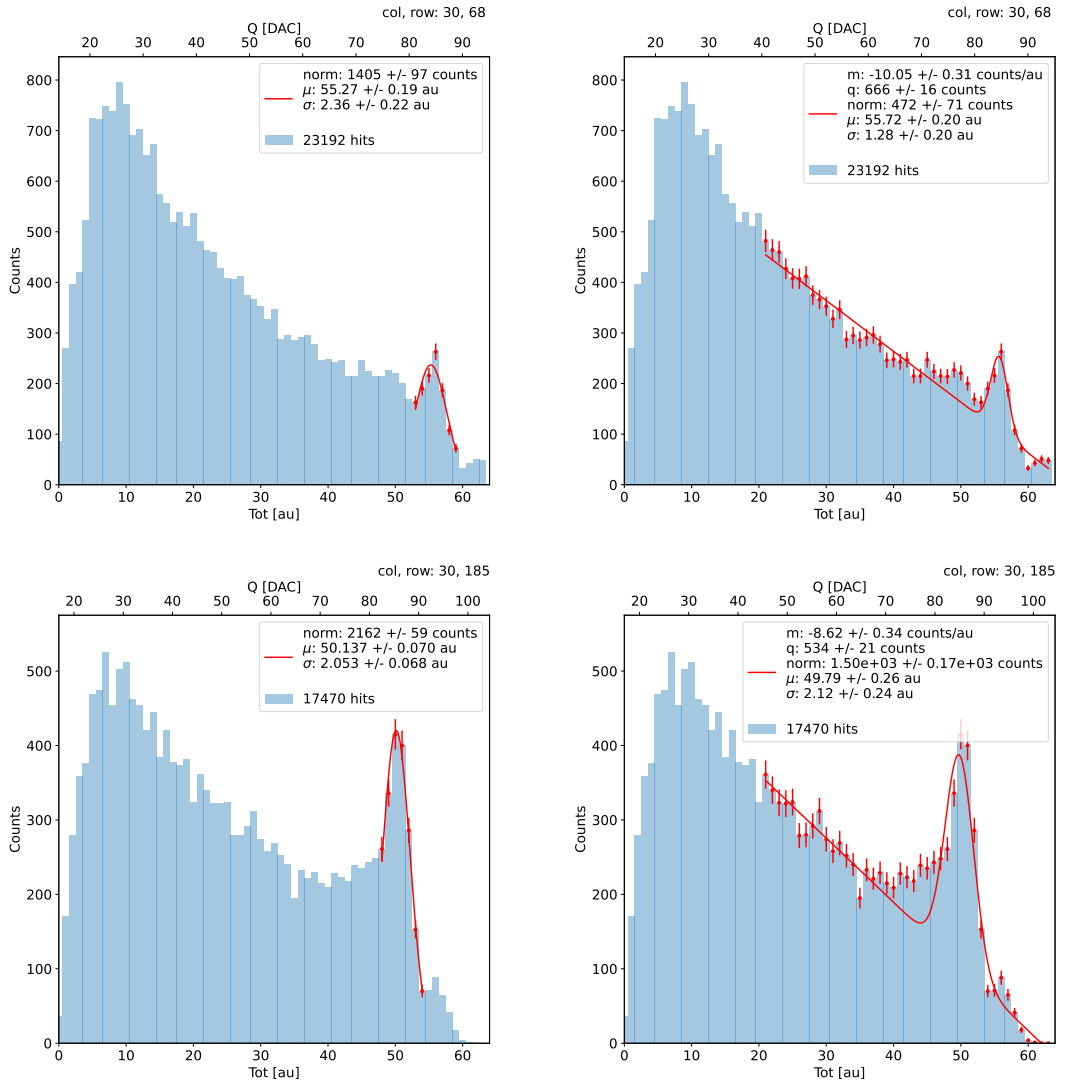


Figure 6.6: due pixel per far vedere la differenza tra i fit. Sottolinea che in rosso ci sono i bin fittati. La doppia scala utilizza le info trovate nel paragrafo precedente per il dato pixel in questione. Per avere una corrispondenza grezza in elettroni basta moltiplicare per 20 e- dac.

1064 the long tail on the left to all the events with partial absorption due to charge sharing
 1065 among neighbors pixels. In order to reduce the charge sharing, the pixel dimension in
 1066 TJ-Monopix2 has been reduced down to **check**. The events on the right side of the peak,
 1067 instead, corresponds to the K_β photons. Looking at the histograms for pixel (30, 185) and
 1068 (30,69) a significant difference in the peak to tail ratio leaps out. This difference in the
 1069 efficiency of detecting the signal can be related with the position of the pixel in the matrix:
 1070 in particular pixels in the upper part of the matrix (rows 112-224) have a more prominent

peak, while in pixels in the lower part (rows 0-111) there is a higher partial absorption. I
 recall now that there is a slightly difference in the structure of the low dose-epi layer (??)
 among the rows in the matrix, in particular pixels in rows 112-224 are supposed to have
 a higher efficiency in the pixel corner.

For the calibration I have need to establish the peak position; to do that I perform a
 fit of the ToT histogram of each pixels. As fit functions I test both the solutions below:

$$f(x, N, \mu, \sigma) = \frac{N}{\sigma\sqrt{2\pi}} e^{-\frac{1}{2}(\frac{(x-\mu)}{\sigma})^2} \quad (6.7)$$

$$f(x, m, q, N, \mu, \sigma) = m x + q + \frac{N}{\sigma\sqrt{2\pi}} e^{-\frac{1}{2}(\frac{(x-\mu)}{\sigma})^2} \quad (6.8)$$

Nel primo caso ho fissato pochi pixel attorno a picco: il range è stato determinato ..

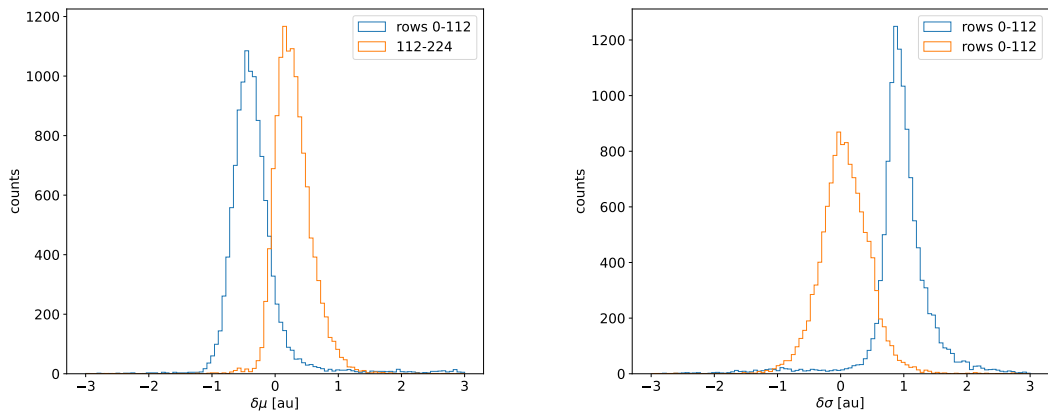


Figure 6.7: Here there are shown the defference between the parameters μ and σ fitted with only a gaussian and with a gaussia plus a line. When $\mu < 0$ the fit function 6.7 has given a worst peak (shifted on the left); when $\sigma < 0$, 6.8 has given a worst peak width (larger sigma)

controlla. Nel secondo caso invece il range è.. Controlla sullo script Even if the difference
 in the peak position between the two cases is not really relevant (6.7) being of the order
 of 0.8-1.5 %, it still introduces a systematic effect moving the peak on the left beacuse of
 the contribution of the tail. Indeed, we know that the sharp edge on the right corresponds
 to the complete absorption of the photon, so excluding the little bump on the right, the
 more the fitted parameter is on the right, the better the fit is. Moreover, there is also

1084 systematic effect on the peak width, infact the worst fit also gives an overestimation of
 1085 the peak width. Even looking at the χ^2 , the fit function 6.7 seems so be the better choise,
 1086 except for a sample of pixels on the lower part of the matrix, the one with lower efficiency.

1087 Mappa del ferro da cui, come descritto enll'equazione si ricava la capacity. La struttura
 1088 a bande della capacità ha origine nel plot... e quindi nella calibrazione. Andando a vedere
 1089 gli istogrammi di queste due variabili si vedono dei picchi. C'è qualche struttura nella
 1090 matrice che condiziona il funzionamento delle righe? Larghezza della gaussiana: fai il
 discorso a cosa contribuisce ad un picco così largo. è compatibile con quanto ti aspetti?

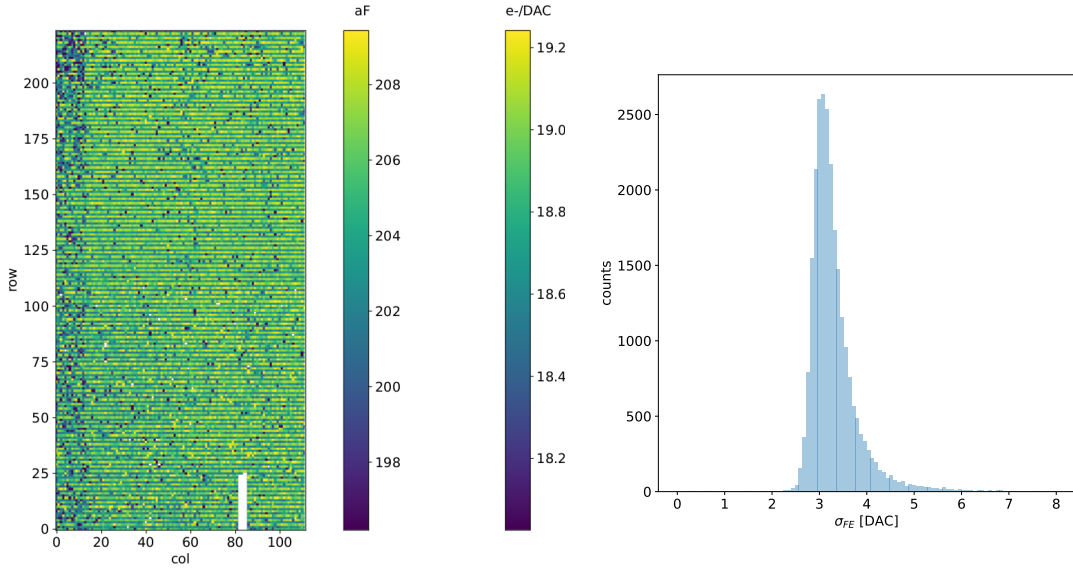


Figure 6.8

1091

1092 6.1.4 PMOS flavor: changing the bias

1093 In order to study the behavior of the sensor changing the bias, I perform some injection
 1094 scans in different configurations. The thickness of the depletion has to be considered
 1095 indeed an important parameters for the efficiency of the signal, and in particular it plays
 1096 an important role if bho, trova qualcosa da dire.

1097 Given that the chip under examination has a gap in the low dose epi-layer (look at
 1098 chapter ??) we were not able to change independently the bias of the substrate (PSUB)
 1099 and of the p-well (PWELL), but they must be kept at the same value, differently from
 1100 other chips, where thay can be changed as reported in figure 4.10. Turning down the bias,
 1101 the depletion region narrows and the efficiency reduces in particular in the pixel corner; La

	-6 V	-3 V	0 V
Threshold [DAC]	20.04 ± 1.6	21.0 ± 1.6	24.5 ± 1.8
Noise [DAC]	0.613 ± 0.075	0.625 ± 0.078	0.822 ± 0.098
Slope [au/DAC]	0.726 ± 0.027	0.707 ± 0.028	0.573 ± 0.021
Offset [au]	-10.8 ± 1.9	-11.2 ± 1.8	-11.1 ± 1.5

Table 6.3: The errors are the standard deviations of the corresponding distributions.

1102 soglia si alza di meno di 1/3, mi sarei aspettata un po' di più guardando il plot. Attenzione
 1103 che il plot non è fatto con un ngap, quindi ci sta che il guadagno lì cali più bruscamente.
 1104 poi non si capisce benissimo dalla colormap. Anche la slope diminuisce di circa meno di
 1105 un terzo. Il noise aumenta leggermente. Il picco del ferro invece si sposta a sinistra di
 1106 un terzo. Lo spostamento è dovuto alla diminuzione del gain, che influisce sul ToT.

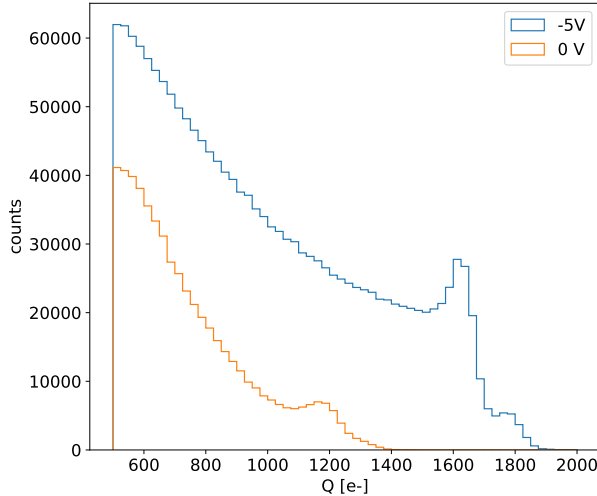


Figure 6.9: With the same acquisition time.

1107 6.1.5 Measurements with radioactive sources

1108 Signal response characterization using radioactive sources and cosmic rays have been made.
 1109 The Sr90 source emits electrons that: lo spettro ha un cutoff a che E?
 1110 conto/plot sulla differenza elettrone sr e mip. The signal generated by electrons is sim-
 1111 ilar to the one generated by minimum ionizing particle (MIPS). The spectrum is expected

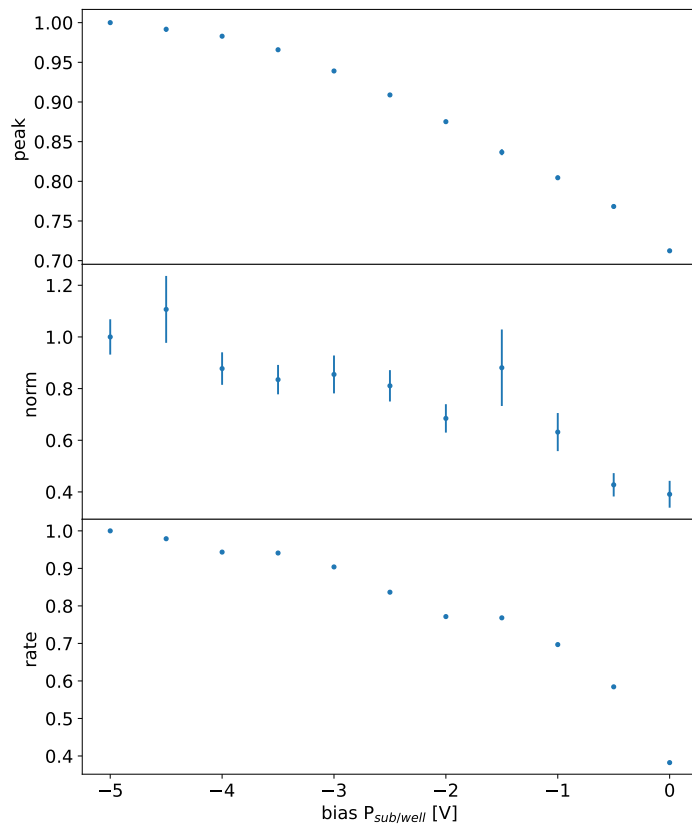


Figure 6.10: da rifare tenendo la sorgente ferma tra un'acquisizione e l'altra

1112 to follow a Langau-Gauss distribution

- 1113 • sommato i cluster Spiega la tua definizione di cluster.

- 1114 • plot dello spettro del ferro convertendo in elettroni per il PMOS flavor e facendo la
1115 somma dei cluster.

- 1116 • di che la tua definizione di cluster è ok perchè sono quasi tutti vicini: plot con la
1117 distanza e qualche stima delle coincidenze casuali.

- 1118 • mappa di qualche evento di cluster sia per Sr che per FE

- 1119 • istogrammi in carica, con carica sommata di Sr e Fe, oer il flavor PMOS dove hai
1120 fatto la calibrazione o per tutti?

1121 Spiega che con il flavor HV abbiamo una perdita di sengnale, fai vedere uno spettro di

1122 delle misure dell'8 marzo.

1123 **6.1.6 Dead time measurements**

1124 The hit loss is due to analog and digital pile up: the first one occurs when a new hit
1125 arrives during the pre-amplifier response, the second instead, which is the more relevant
1126 contribution with high rate, while the information of the previous hit has not yet been
1127 transferred to the periphery. As only one hit at a time can be stored on the pixel's RAM,
1128 until the data have completed the path to get out, the pixel is paralyzed and the dead time
1129 τ almost corresponds with the time needed to transmit the data-packets off-chip. Since the
1130 exportation of data from pixel to the EoC occurs via a 21-bits data bus, only one clock
1131 cycle is needed to transfer the data to the end of column and the dead time bottleneck is
1132 given by the bandwidth of the serializer at the EoC. In our setup the serializer operates
1133 at 40 MHz, thus to transmit a data packet (27-bit considering the addition at the EoC)
1134 at least 675 ns are needed. For what we have said so far, the R/O is completely sequential
1135 and therefore is expected a linear dependence of the reading time on the number of pixels
1136 to read:

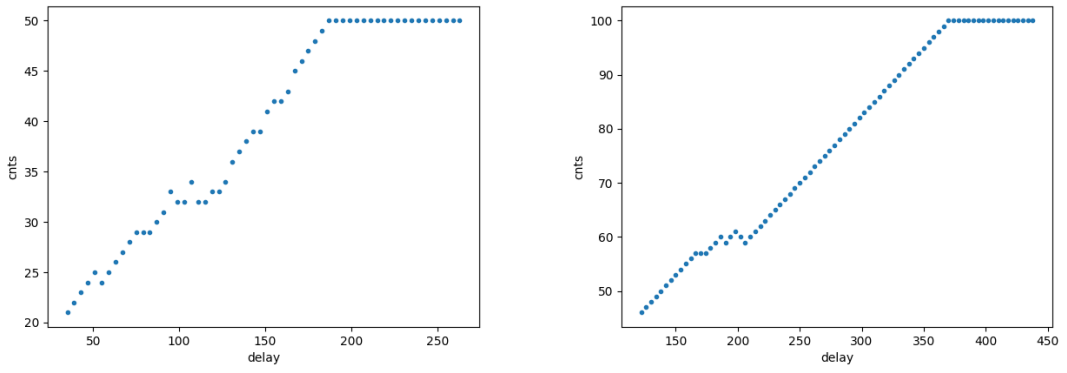
$$\tau = 25 \text{ ns} \times (\alpha N + \beta) \quad (6.9)$$

1137 where α and β are parameters dependent on the readout chain setting.

1138 To measure and test the linearity of the reading time with the number of pixels firing,
1139 I have used the injection mode available on the chip. Indeed, the injection mode allows
1140 fixing not only the amplitude of the pulse, which corresponds to the charge in DAC units,
1141 but also the period and the width. I have injected a fix number of pulses (100) and looked
1142 for the rate when the efficiency decreases. Moreover to test that there is no dependence of
1143 the digital readout time from the charge of the pulse, I have tried to change the amplitude of
1144 the pulse injected, but the parameters found were consistent with the default configuration
1145 ones.

1146 Al posto degli esempi con 5 e 10 pixels metterei un esempio dell'efficienza vs il periodo
1147 quando leggo un singolo pixel. Una cosa che volevo fare era anche provare a fissare la slope
1148 con cui l'efficienza scende: se la slope è uguale per tutti il readout diventa completamente
1149 predittivo.

1150 While the single pixel reading time and the dead time do not depend on the position
1151 on the pixel matrix and are equal to 106 (46+60) clock counts within 1 clock count, on



(a) efficiency vs DELAY 5 pixels

(b) efficiency vs DELAY per 10pixels

Parameter	Value [DAC]	Value [μ s]
START_FREEZE	64	1.6
STOP_FREEZE	100	2.5
START_READ	66	1.65
STOP_READ	68	1.7

Table 6.4: Default configuration of the R/O parameters

the other hand the τ depends on the pixel position on the matrix when more than one pixel are firing. In particular the priority chain goes from row 224 to row 0, and from col 0 to 112, that means the last pixels to be read is the one on le bottom right corner of the matrix.

In figure 6.13 is reported the reading time versus the number of pixels injected; the R/O parameters that control the reading time and their default values are reported on table ??.

The factor α , referring to eq. 6.9 is proportional to the difference (STOP_FREEZE - START_READ), while the offset β lies between 5 and 15 clock counts. Since through the injection a random hit rate on the matrix can't be simulated, as the coordinates of the pixels to inject must be specified, for convenience I used the pixels on the same column/row. No difference in the α and β coefficients has been observed between the two case.

Ci sarebbe da spiegare perchè i parametri che usiamo noi come default non sono quelli

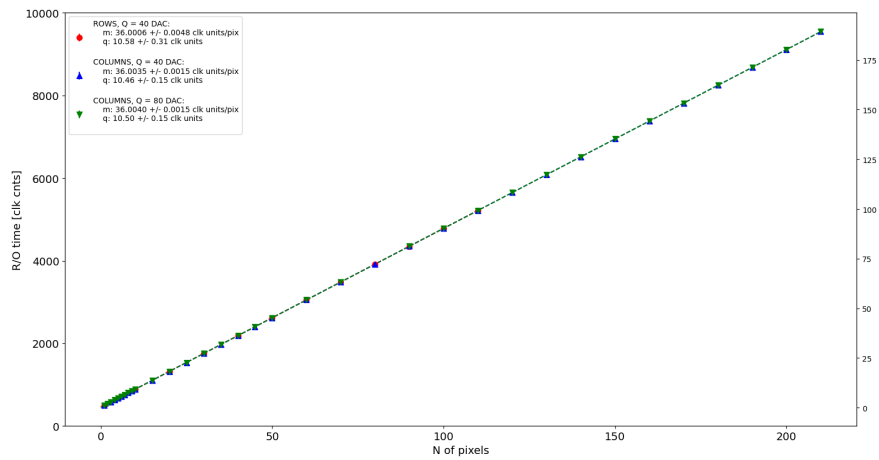


Figure 6.12

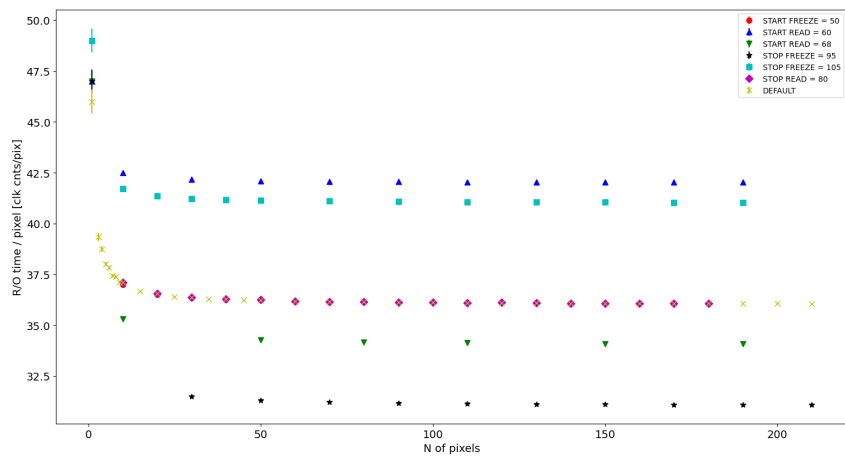


Figure 6.13

1166 che minimizzano il tempo di lettura. La spiegazione è che "Abbiamo copiato i valori
 1167 dal repository di quelli di Bonn". Un'altra domanda potrebbe essere: come mai non ho
 1168 esplorato una zona più vasta per i parametri del R/O. Cambiando molto i parametri del
 1169 R/O la lettura non funzionava per niente: ad esempio CONF_STOP_FREEZE non può
 1170 essere impostato né sopra 105 né sotto 95

1171 6.2 ARCADIA-MD1 characterization

₁₁₇₂ **Chapter 7**

₁₁₇₃ **Test beam measurements**

₁₁₇₄ At PRF smaller than 100 Hz, all the dosimeters analyzed have a shorter signal collection
₁₁₇₅ time with respect to the repetition time of the pulses (maggiore uguale 10 ms), and,
₁₁₇₆ consequently, the saturation is influenced only by the dose-per-pulse (duration of the
₁₁₇₇ pulse is around 2.5 us)

₁₁₇₈ During August 2022 a testbeam took place in Santa Chiara hospital in Pisa, where a
₁₁₇₉ new accelerator designed for both medical research and R&D in FLASH-RT, and for this
₁₁₈₀ reason called "ElectronFlash", have been installed a few months ago.

₁₁₈₁ The motivation of the testbeam measurements were testing TJ-Mopopix1 in condition
₁₁₈₂ different from the one foreseen during the design and also testing the mechanical and the
₁₁₈₃ DAQ setup for other future measurement. TJ-Monopix1 is supposed to be employed for
₁₁₈₄ tracking in HEP experiments while our goal was testing the possibility of integrating the
₁₁₈₅ charge released by more particles at ultra high hit rate achievable with the accelerator.

₁₁₈₆ **Una frase di disclaimer sul fatto che non siamo riusciti a testare quello che volevamo.**

₁₁₈₇ In medical physics the dose is indeed the standard parameter to characterize the beam
₁₁₈₈ because of its obvious relation with the damage caused in the patient: firstly the oncolo-
₁₁₈₉ gists prescribe a certain dose taking into account the efficacy of the treatment and then
₁₁₉₀ the medical physicists, on the basis of simulations, decide the energy and the intensity of
₁₁₉₁ the beams to dispense the prescribed dose amount. By the point of view of the instrumen-
₁₁₉₂ tation and the testing on it, a more common and useful parameter is instead the rate or
₁₁₉₃ the fluence of particles. The conversion between the two quantity can be found thinking to
₁₁₉₄ the definition of dose: it is the concentration of energy deposited in tissue as a result of an

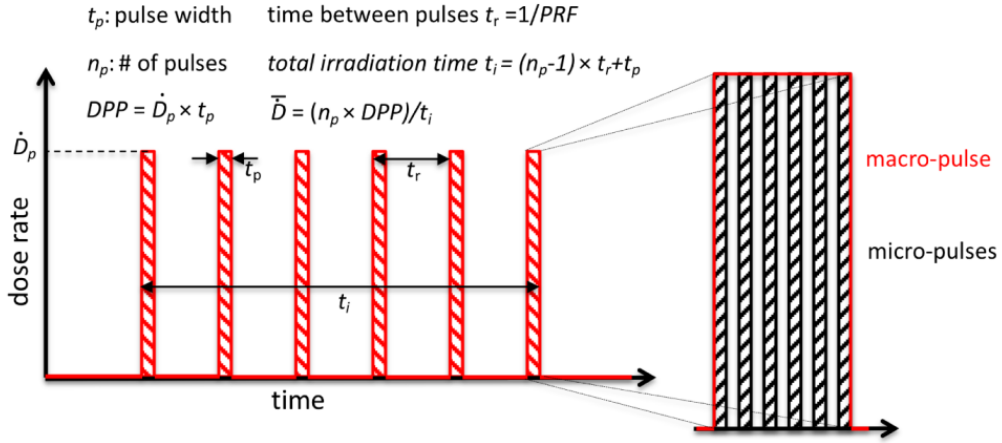


Figure 7.1: Typical beam structure of a beam with the standard characteristic quantity

1195 exposure to ionizing radiation. Assuming total absorption of electrons in water, defined
 1196 by law as the ordinarily reference medium, the dose can be expressed as:

$$D[Gy] = \frac{NE[eV]}{\rho[g/cm^3]A[cm^2]x[cm]} \quad (7.1)$$

1197 After having applied the conversion of the energy from eV to J and noticed that $E/\rho x$
 1198 roughly corresponds to the stopping power S of electrons in water, a simple estimation of
 1199 the dose released in water is:

$$D[Gy] = 1.602 \cdot 10^{-10} N[cm^{-2}] S[MeV cm^2/g] \quad (7.2)$$

1200 7.1 Apparatus description

1201 The accelerator is placed in a bunker inside the hospital: to shield the outdoor from
 1202 ionizing radiation the bunker has very thick walls of cementum and both the control units
 1203 of the accelerator and of the detector were placed outside the bunker. For practicability
 1204 reasons the power supply were the only device to be placed inside the bunker.

1205 7.1.1 Accelerator

1206 The ElectronFlash accelerator is an electron Linear Accelerator (LINAC) with two energy
 1207 configurations, at 7 MeV and 9 MeV, and it can reach ultra high intensity (40 Gy/pulse)
 1208 keeping the possibility of accessing many different beam parameters and changing them
 1209 independently from each other. This characteristic is fundamental for research in FLASH-
 1210 RT, both for the medical aspects and for the studies on detectors; for example is not really

\bar{D}	Dose rate (mean dose rate for a multi-pulse delivery)	0.005-10000 Gy/s
\dot{D}	Intra pulse dose rate (dose rate in a single pulse)	0.01-1 10^6 Gy/s
DDP	Dose in a single pulse	0.04-40 Gy
PRF	Pulse repetition frequency(number of pulses delivered per unit of time)	1-350 Hz
t_p	Pulse width	0.2-4 μ s
n	Number of pulses	single/pulse train

Table 7.1: The parameters that can actually be set by the control unit are the PRF, DDP, t_p and n (in particular singolar irradiation or pulse train), while the other changes consequently.

1211 clear the dependence of the efficacy of the FLASH effect on the whole dose parameters.
 1212 ElectronFlash is **almost the only one** in the world having this charateristic, **ricontrolla sulla**
 1213 **review, c'era qualcosa che puoi dire.** The accelerator implements a standard beam struc-
 1214 ture for RT with electrons (fig. 7.1), that is a macro pulse divided in many micropulses;
 1215 the parameters used to set the dose and their range of values settable by the control unit
 1216 is reported in table 7.1.

1217 The accelerator is provided of a set of triod cannons \sim 1.2 m long and with diameters
 1218 from 1 cm to 12 cm and a collimator that can be used as beam shaper to produce a
 1219 squircle shape. The triode, which is made by plexiglass, must be fix to the gun during the
 1220 irradiation and is needed for producing an uniform dose profile (fig.7.2) which is desired
 1221 for medical pourpose via the scattering of electrons with the plexiglass.

1222 7.1.2 Mechanical carriers

1223 The tested detector consists in one chip, the Device Under Test (DUT), mounted on a
 1224 board and connected to FPGA with same arrangement of figure 7.7. These have been
 1225 positioned vertically in front of the triode on a table specifically built for the testbeam.
 1226 The tree board have been enclosed in a box of alluminium with a window on the DUT
 1227 and with the required holes at the side to enable the biasing via cables and the connection
 1228 with the DAQ provided via ethernet cable. A trigger signal coming from the control unity
 1229 and syncronize with the pulses emitted from the beam has been also sent to the FPGA.

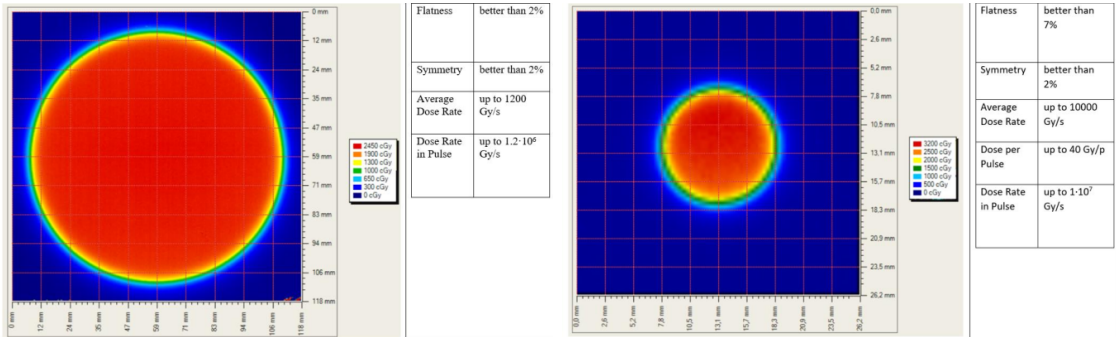


Figure 7.2: Two example of x-y isodose curves for two different triodes, 10 cm and 1 cm respectively, reported by the producer in the manual with the specific of the accelerator (S.I.T. - Sordina IORT Technologies S.p.A.). With the smaller collimator the dose rate in pulse is comparatively higher.

1230 This signal cannot be considered a trigger signal, since being a prototypes TJ-Monopix1
 1231 has been designed to be triggerless, but the time of arrival of this signal, which is saved
 1232 by the FPGA, can allow the reconstruction of the of the arrival of the bunch during the
 1233 analysis.

1234 In order to shield the sensor from the whole particles emitted from the gun, two
 1235 alluminium collimators have been fabricated: one has been positioned at the triode exit
 1236 while the other in front of the DUT. The collimators are $t=32$ mm thick and have a
 1237 diameter d equal to 1 mm: assuming a beam divergence bigger than $d/t=1/32 = 1.8^\circ$,
 1238 which is the case, the collimator at the triode output was supposed to work as a point
 1239 source and to reduce the rate on the DUT of a factor at least $4 \cdot 10^{-4}$. The second one,
 1240 being near the DUT, was instead supposed to shield the sensor from the electrons which
 1241 have passed the first one, except for a region of 1 mm^2 configurable using [come si chiamano](#)
 1242 [quei cacciavitini per settare la posizione?](#).

1243 7.2 Measurements

1244 Because of the dead time of TJ-Monopix1 it is not possible resolving the bunch sub-
 1245 structure and almost no one pixel can read more than a hit per bunch. I recall, indeed,
 1246 that the dead time per pixel depends on the location on the priority chain for the readout
 1247 and for each pixel $\lesssim 1 \mu\text{s}$ (fig. 7.7) are needed; therefore only a few pixels at the top of

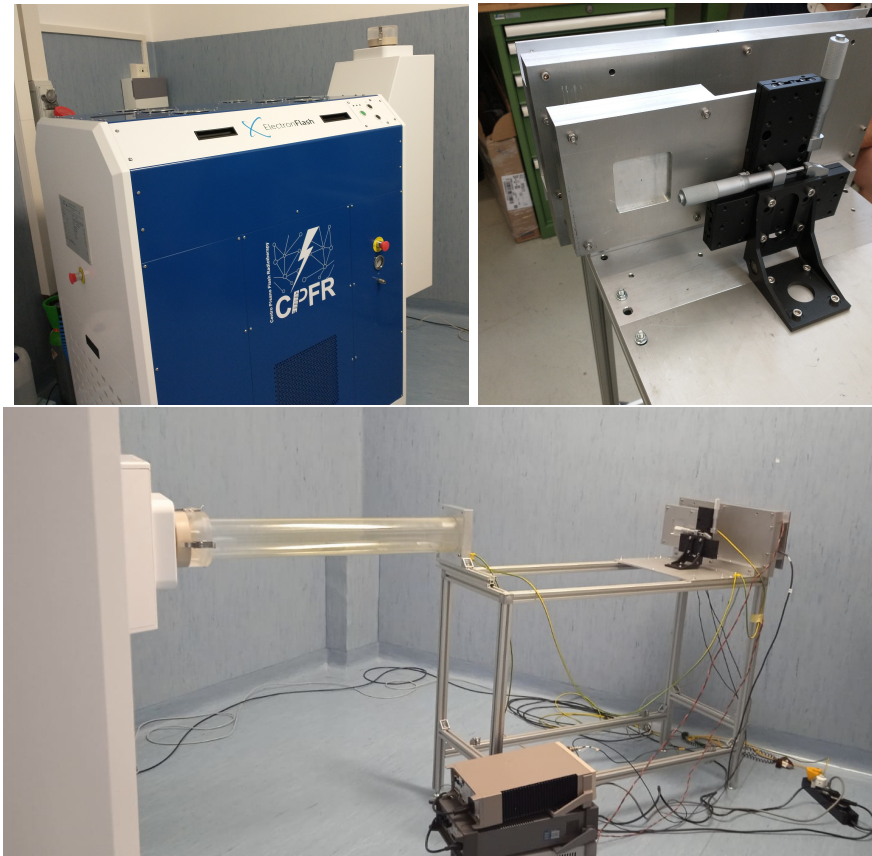


Figure 7.3: Experimental set up. (a) Electron flash accelerator: gantry rotante che consente un orientamento del fascio da 0° a 90° (orizzontale / verticale) in tempo reale monitorato da un inclinometro integrato. (b) Collimator and DUT box. (c) Whole structure: we used the 10 cm diameter and 1.2 m long triode; the DUT which is in the box behind the two collimators is connected to the power supply units.

1248 the priority chain (at the upper left of the matrix) can fire a second time, since they in
 1249 principle can be read the first time before the end of the pulse (assuming a pulse duration
 1250 in $2\ \mu\text{s}$ - $4\ \mu\text{s}$) and then can be hit again.

1251 Since resolving the single electron track is impossible, a way this sensor could be used
 1252 in such context is reducing its efficiency and taking advantage of the analog pile up and
 1253 of the linearity of the analog output (ToT), in order to see a signal produced not by the
 1254 single particle but by more electrons. Reducing the efficiency and the sensibility of the
 1255 sensor is essential in order to decrease the high charge signal produced in the epitaxial
 1256 layer: if the sensor is completely depleted the collection efficiency is closer to 1% and if the

whole charges produced by a MIP, $80 \text{ e-}/\mu\text{m}$ about, are collected, the saturation limit is soon reach. Then a condition where there is a partial recombination of the center electron-hole created in the bulk is desiderable. On the other hand, the smaller the output signal value and the higher the rate the detector can cope with: indeed, the rollover constitutes a limit for the usage of the analog output. With the standard configuration of the FE parameters and the epitaxial layer completely depleted, a MIP produces a ToT out of range of representation of 6-bit; so as to obtain smaller output signals one can operate on the reduction of the gain of the preamplifier or on the pulse velocity of returnig to the baseline. Recalling the results in section 6.1.4, I have shown that concerning the PMOS flavor 1, reducing the bias from -6 V to 0 V brings a reduction of efficiency down to 40 %, and a reduction in the gain of a factor $\sim 1/3$, while the reduction of the gain of the preamplifier allows a reduction of **circa 10, ma da controllare.**

In order to taking advantage of the analog pile up and integrating the charge, for semplicity assume of two electrons, the second one must hit the pixel before the ToT goes under the threshold. The general condition is then $\overline{\Delta T} < \overline{ToT}$, but if a high $P_\mu(n \geq 1)$ is required, a lower $\overline{\Delta T}$ may be desired:

$$P(n \geq 1) = \sum_{n=1}^{\infty} \frac{e^{-\mu} \mu^n}{n!} = 1 - P(0) = 1 - e^{-\mu} \quad (7.3)$$

$$\mu = \frac{\overline{ToT}}{\overline{\Delta T}} \quad (7.4)$$

If a $P_\mu(n \geq 1) = 99\%$ then the $\overline{\Delta T}$ must be $\sim 0.22 \overline{ToT}$. The ToT is in range [0,64] but since the rollover must be avoided, the \overline{ToT} must be lower than 32, and then the minimum rate on the pixel must be 1.25 MHz.

During the testbeam many runs have been performed, spanning the energy, the dose per pulse and the four possible configurations with/without the collimators. We have used the PMOS flavor 1 in the standard configuration: we have biased the PWELL and PSUB at -6 V and set the standard default FE parameters reported in table ???. During all the acquisitions we have used pulses with t_p of 4 μm and with the smallest PRF settable, which is 1 Hz, in order to start in the most conservative working point exluding the digital pile up of events from different bunch: even if the whole matrix turns on and there are 25000

1285 hits, the total readout time corresponding to 25 ms is still lower than the time between two
1286 consecutive pulses. The readout starts with the trailing edge of the first pulse going down
1287 the threshold, ~ 50 clk = 1.25 μ s after this moment the FREEZE signal is sent to the whole
1288 matrix, and the transmission of the data to the EoC begins. The hits read are the ones
1289 whose TE occurred during the 50 clk counts; the ones, instead, whose TE occur during the
1290 FREEZE are stored in the pixel memory and read during a second readout. Obviously
1291 since the readout of the first sub-pulse finishes much later than the bunch ends up, each
1292 pixel can store only one hit. An example of the two sub-pulses is shown in figure ??:
1293 in the acquisition we injected 5 pulses with both the collimators mounted on the table.
1294 Looking at the spectrum **si vede che lo spettro del secondo pulse ha una coda più lunga a**
1295 **destra: questo è dovuto al fatto che le hit con tot lungo hanno il TE che cade durante il**
1296 **FREEZE e quindi vengono lette durante il secondo impulso.** On the other hand the 2D
1297 histograms, being uniform and not showing discontinuities, suggest that the collimators
1298 do not shield all the particles: this was due to a photon background higher than expected.
1299 When we have put aside the collimators, instead, the fluence was too high that the whole
1300 matrix turns on in 50 clk counts; then the 2 pulses substructure no more appears (fig. 7.6).

1301 CONTROLLA PERCHÈ PORTEBBE ESSERE UNA CAZZATA

1302 After the testbeam a simulation of the emission of electrons from the accelerator and
1303 their path across the triode and the collimators has been developed via Geant-4 **come si**
1304 **ringrazia il lavoro di qualcuno in maniera formale?** The high background we saw although
1305 the collimators were mainly produced by electrons Bremsstrahlung during the transition
1306 through the aluminium collimators. **dalla simulazione si è visto che nessun elettrone**
1307 **arriva sul chip quando ci sono montati i collimatori, mentre nel caso senza collimatori gli**
1308 **eventi sono sostanzialmente tutti elettroni (frazione di fotoni prodotti in aria è?).** The
1309 photons' simulated spectrum in the three configurations are shown in figure ?? **confronto**
1310 **con quello che vedo nello spettro sopra: dati.**

1311 • plot n di eventi che vedo con le diverse configurazioni

1312 • simulazione surya

1313 • confronta con misure dello spettro che vediamo senza e con collimatori.

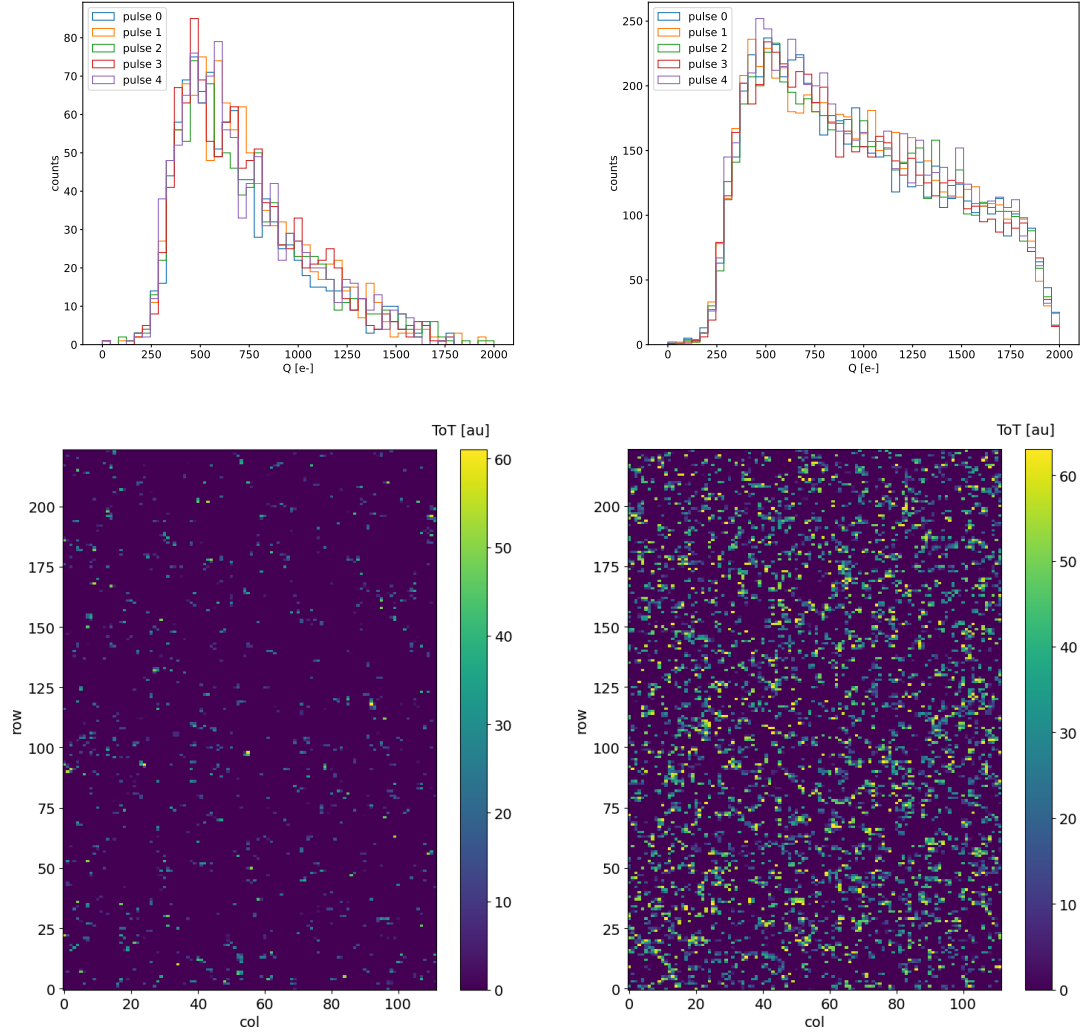


Figure 7.4: Acquisition with both the collimators: 5 pulses at DDP=0.07 Gy. (a) Spectrum of the charge released in the sensor: to apply the conversion I used the information found in the previous chapter. (b) 2D histogram of the ToT of the hits arrived in the sub-pulses.

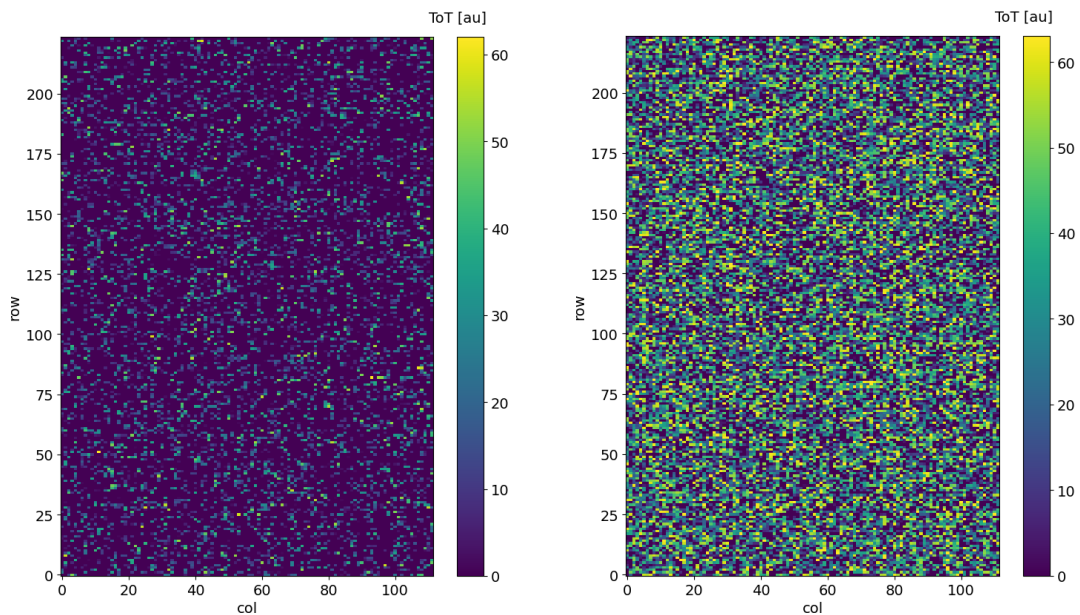


Figure 7.5: Acquisition with both the collimators: 5 pulses at $DDP=0.6\text{ Gy}$. 2D histogram of the ToT of the hits arrived in the sub-pulses. Compared with the previous maps, since the DDP is much higher, more pixels turn on.

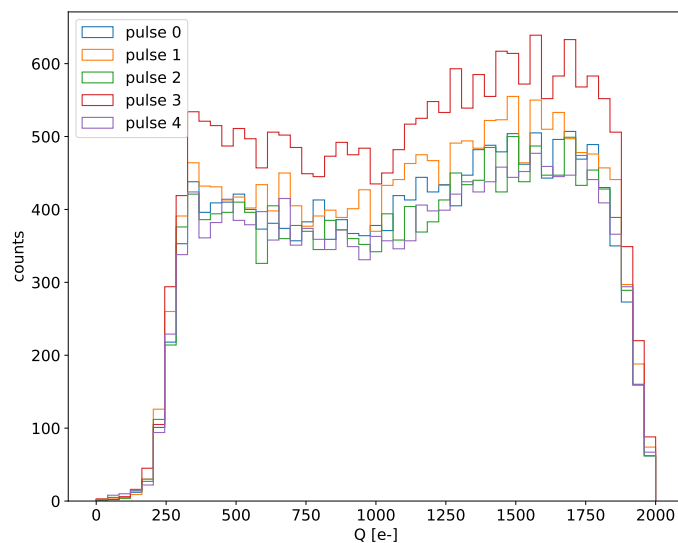


Figure 7.6: Acquisition without any collimator: 5 pulses at $DDP=0.04\text{ Gy}$.

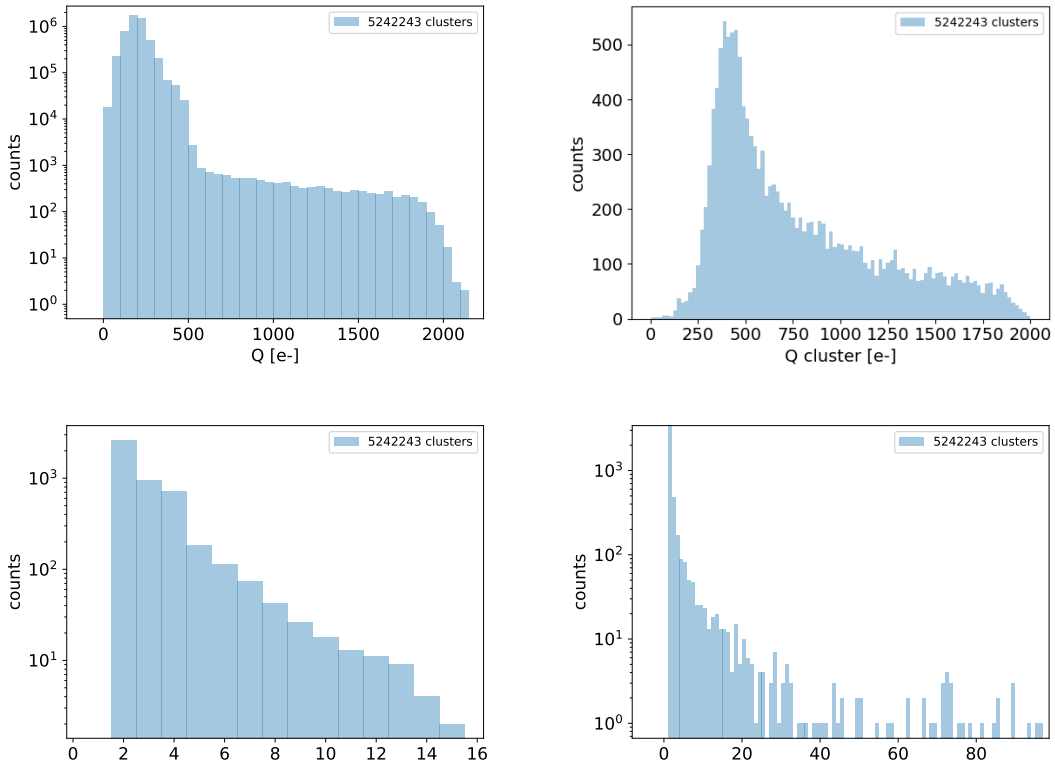


Figure 7.7: plot dei raggi cosmici da rigenerare

¹³¹⁴ 7.2.1 MIP spectrum using cosmic rays as source

¹³¹⁵ Since a MIP should produce about 2 ke- in the epitaxial layer, it should provide a signal
¹³¹⁶ that in our conditions (full depletion and high gain) rolls over: in this situation making
¹³¹⁷ prediction on the spectrum expected for MIPs becomes hard. Therefore, in order to
¹³¹⁸ compare the spectrum observed at the testbeam with one certainly produced by MIP I
¹³¹⁹ have made some acquisitions without any radioactive source, in order to look at the cosmic
¹³²⁰ ray events. To be confident with having selected MIPs from cosmic rays and cut the noise, I
¹³²¹ have selected only the events with multiple hits: these events are mainly clusters produced
¹³²² by the same impinging particle since the random coincidence probability is very low. In
¹³²³ fact the cosmic rays and noise rates on the whole matrix are respectively 0.02 Hz and
¹³²⁴ $\sim\text{Hz}$, the dead time in such a low occupancy condition can be always approximated with
¹³²⁵ $1\text{ }\mu\text{m}$ (this is not completely true for multiple hits events for which the priority chain
¹³²⁶ should be considered), the random coincidence rate is 10^{-8} Hz . Come mai lo spettro in
¹³²⁷ lab è diverso da quello visto con gli elettroni da 9 MeV al santa chiara? Chiedi a Surya il

1328 rate visto sul detector senza collimatori.

₁₃₂₉ **Appendix A**

₁₃₃₀ **Pixels detector: a brief overview**

₁₃₃₁ **A.1 Radiation damages**

₁₃₃₂ Radiation hardness is a fundamental requirement for pixels detector especially in HEP
₁₃₃₃ since they are almost always installed near the interaction point where there is a high
₁₃₃₄ energy level of radiation. At LHC the ϕ_{eq} per year in the innermost pixel detector is
₁₃₃₅ $10^{14} n_{eq}/cm^2$; this number reduces by an order passing to the outer tracker layer [2] pag
₁₃₃₆ 341 Wermes. Here the high fluence of particles can cause a damage both in the substrate
₁₃₃₇ of the detector and in the superficial electronics.

₁₃₃₈ The first one has a principal non ionizing nature, due to a non ionizing energy loss
₁₃₃₉ (NIEL), but it is related with the dislocation of the lattice caused by the collision with
₁₃₄₀ nuclei; by this fact the NIEL hypothesis states that the substrate damage is normalized to
₁₃₄₁ the damage caused by 1 MeV neutrons. Differently, surface damages are principally due
₁₃₄₂ to ionizing energy loss.

₁₃₄₃ **DUE PAROLE IN PIÙ SUL SURFACE DAMAGE** A charge accumulation in oxide
₁₃₄₄ (SiO_2) can cause the generation of parasitic current with an obvious increase of the 1/f
₁₃₄₅ noise. Surface damages are mostly less relevant than the previous one, since with the de-
₁₃₄₆ velopment of microelectronics and with the miniaturization of components (in electronic
₁₃₄₇ industry 6-7 nm transistors are already used, while for MAPS the dimensions of compo-
₁₃₄₈ nents is around 180 nm) the quantity of oxide in circuit is reduced.

₁₃₄₉ Let's spend instead two more other words on the more-relevant substrate damages:
₁₃₅₀ the general result of high radiation level is the creation of new energy levels within the

1351 silicon band gap and depending on their energy-location their effect can be different, as
1352 described in the Shockely-Read-Hall (SRH) statistical model. The three main consequence
1353 of radiation damages are the changing of the effect doping concentration, the leakage
1354 current and the increasing of trapping probability.

1355 **Changing of the effective doping concentration:** is associated with the cre-
1356 ation/removal of donors and acceptors center which trap respectively electrons/holes from
1357 the conduction band and cause a change in effective space charge density. Even an in-
1358 version (p-type becomes n-type¹) can happen: indeed it is quite common at not too high
1359 fluences ($\phi_{eq} 10^{12-13} n_{eq} cm^{-2}$). A changing in the doping concentration requires an adjust-
1360 ment of the biasing of the sensor during its lifetime (eq.2.2) and sometimes can be difficult
1361 keeping to fully deplete the bulk.

1362 **Leakage current:** is associated with the generation-recombination centers. It has
1363 a strong dependence with the temperature ($I_{leak} \propto T^2$), whose solution is therefore to
1364 operate at lower temperature.

1365 **Increase of trapping probability:** since the trapping probability is constant in the
1366 depleted region, the collected charge decreases exponentially with the drift path. The
1367 exponential coefficient, that is the mean trapping path, decreases after irradiation and
1368 typical values are 125-250 μm and must be compared with the thickness of the depleted
1369 region which () corresponds to the mean drift path.

1370 Different choices for substrate resistivity, for junctions type and for detector design are
1371 typically made to fight radiation issues. Some material with high oxygen concentration
1372 (as crystal produced using Czochralki (Cz) or float-zone (Fz) process (**CONTROLLA**
1373 **LA DIFFERENZA TRA I DUE**)) for example, show a compensation effect for radiation
1374 damage; another example is the usage of n+ -in-p/n sensors (even if p+ -in-n sensors are
1375 easier and cheaper to obtain) to get advantage of inversion/to have not the inversion (since
1376 they are already p-type). After inversion the n+p boundary, coming from n+ in-n, but to
1377 keep using the sensor the depletion zone still must be placed near the diode.

1378 **Single Event Upset, in sostanza è quando un bit ti cambia valore (da 0 a 1 o viceversa)**
1379 **perché una particella deposita carica nell'elettronica che fa da memoria registro/RAM/....**

¹L'INVERSIONE OPPOSTA NON CE L'HAI PERCHÈ?

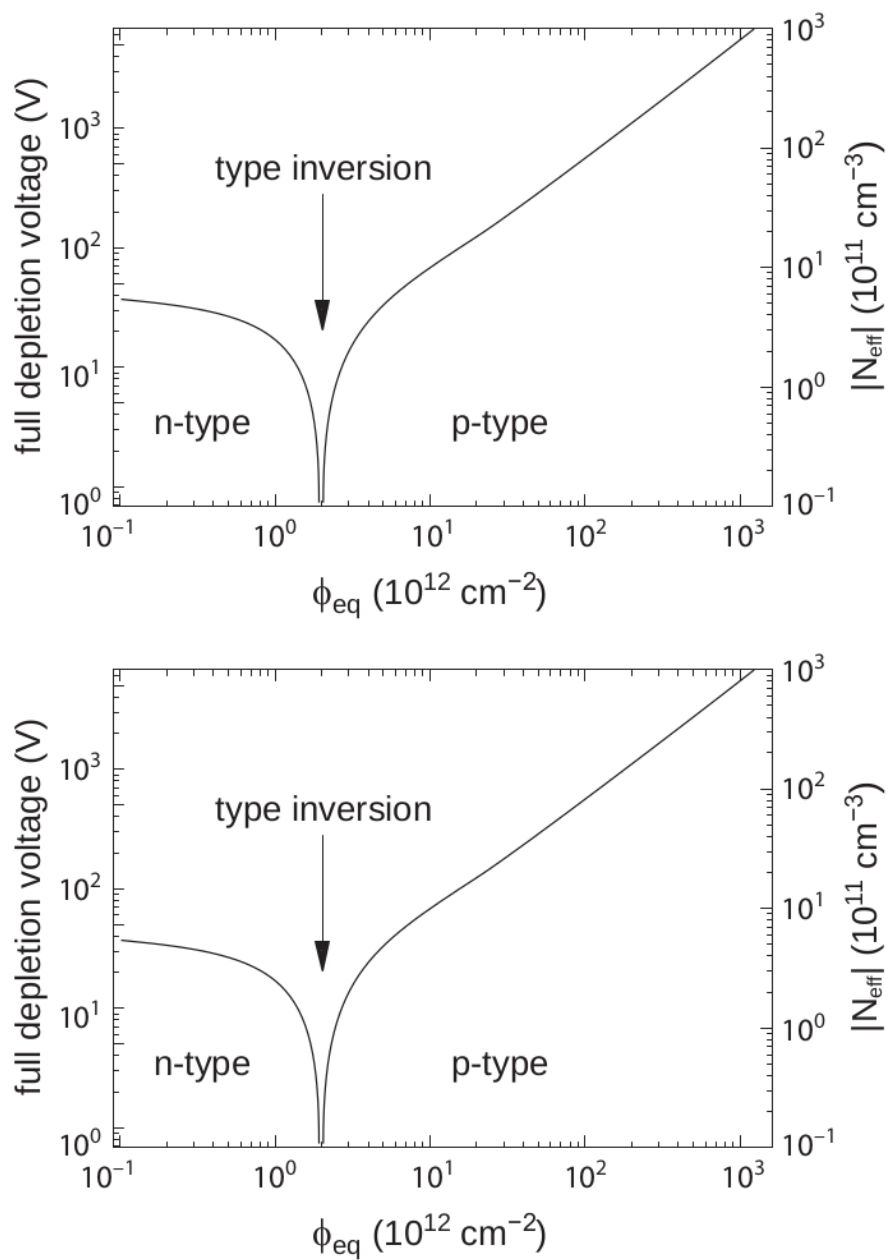


Figure A.1: 1b

1380 Questo tipo di elettronica ha bisogno di un sacco di carica prima che il bit si "flippi"
1381 (cambi valore), infatti tipicamente per avere un SEU non basta una MIP che attraversa
1382 esattamente quel pezzo di chip in cui è implementata la memoria, ma un adrone che faccia
1383 interazione nucleare producendo più carica di quanto farebbe una MIP. Questo metodo pur
1384 essendo più comodo richiede less amount of area ha però come drawback che il registro può
1385 essere soggetto a SEU problema non trascurabile in acceleratori come HL-LHC adronici

¹³⁸⁶ Bibliography

- ¹³⁸⁷ [1] W. Snoeys et al. “A process modification for CMOS monolithic active pixel sensors
¹³⁸⁸ for enhanced depletion, timing performance and radiation tolerance”. In: (2017).
¹³⁸⁹ DOI: <https://doi.org/10.1016/j.nima.2017.07.046>.
- ¹³⁹⁰ [2] H. Kolanoski and N. Wermes. *Particle Detectors: Fundamentals and Applications*.
¹³⁹¹ OXFORD University Press, 2020. ISBN: 9780198520115.
- ¹³⁹² [3] E. Mandelli. “Digital Column Readout Architecture for 10.1109/NSSMIC.2009.5402399
¹³⁹³ the ATLAS Pixel 0.25 um Front End IC”. In: (2002).
- ¹³⁹⁴ [4] M. Garcia-Sciveres and N. Wermes. “A review of advances in pixel detectors for
¹³⁹⁵ experiments with high rate and radiation”. In: (2018). DOI: <https://doi.org/10.1088/1361-6633/aab064>.
- ¹³⁹⁷ [5] C. Marinas. “The Belle-II DEPFET pixel detector: A step forward in vertexing in the
¹³⁹⁸ superKEKB flavour factory”. In: (2011). DOI: [doi:10.1016/j.nima.2010.12.116](https://doi.org/10.1016/j.nima.2010.12.116).
- ¹³⁹⁹ [6] J. Baudot. “First Test Results Of MIMOSA-26, A Fast CMOS Sensor With Inte-
¹⁴⁰⁰ grated Zero Suppression And Digitized Output”. In: (2010). DOI: [doi:10.1109/NSSMIC.2009.5402399](https://doi.org/10.1109/NSSMIC.2009.5402399).
- ¹⁴⁰² [7] A. Dorokhov. “High resistivity CMOS pixel sensors and their application to the
¹⁴⁰³ STAR PXL detector”. In: (2011). DOI: [doi:10.1016/j.nima.2010.12.112](https://doi.org/10.1016/j.nima.2010.12.112).
- ¹⁴⁰⁴ [8] Giacomo Contin. “The STAR MAPS-based PiXeL detector”. In: (2018). DOI: <https://doi.org/10.1016/j.nima.2018.03.003>.
- ¹⁴⁰⁶ [9] Nolan Esplen. “Physics and biology of ultrahigh dose-rate (FLASH) radiotherapy:
¹⁴⁰⁷ a topical review”. In: (2020). DOI: <https://doi.org/10.1088/1361-6560/abaa28>.

- 1408 [10] Fabio Di Martino et al. “FLASH Radiotherapy With Electrons: Issues Related to
1409 the Production, Monitoring, and Dosimetric Characterization of the Beam”. In:
1410 *Frontiers in Physics* 8 (2020). ISSN: 2296-424X. DOI: 10.3389/fphy.2020.570697.
1411 URL: <https://www.frontiersin.org/articles/10.3389/fphy.2020.570697>.
- 1412 [11] M. Dyndal et al. “Mini-MALTA: Radiation hard pixel designs for small-electrode
1413 monolithic CMOS sensors for the High Luminosity LHC”. In: (2019). DOI: <https://doi.org/10.1088/1748-0221/15/02/p02005>.
- 1415 [12] M. Barbero. “Radiation hard DMAPS pixel sensors in 150 nm CMOS technology
1416 for operation at LHC”. In: (2020). DOI: <https://doi.org/10.1088/1748-0221/>
1417 15/05/p05013.
- 1418 [13] K. Moustakas et al. “CMOS Monolithic Pixel Sensors based on the Column-Drain
1419 Architecture for the HL-LHC Upgrade”. In: (2018). DOI: <https://doi.org/10.1016/j.nima.2018.09.100>.
- 1421 [14] I. Caicedo et al. “The Monopix chips: depleted monolithic active pixel sensors with
1422 a column-drain read-out architecture for the ATLAS Inner Tracker upgrade”. In:
1423 (2019). DOI: <https://doi.org/10.1088/1748-0221/14/06/C06006>.
- 1424 [15] D. Kim et al. “Front end optimization for the monolithic active pixel sensor of the
1425 ALICE Inner Tracking System upgrade”. In: *JINST* (2016). DOI: doi:10.1088/
1426 1748-0221/11/02/C02042.
- 1427 [16] L. Pancheri et al. “A 110 nm CMOS process for fully-depleted pixel sensors”. In:
1428 (2019). DOI: <https://doi.org/10.1088/1748-0221/14/06/c06016>.
- 1429 [17] L. Pancheri et al. “Fully Depleted MAPS in 110-nm CMOS Process With 100–300-
1430 um Active Substrate”. In: (2020). DOI: 10.1109/TED.2020.2985639.